Journal of Power Sources 201 (2012) 204–218

Contents lists available at SciVerse ScienceDirect

Journal of Power Sources

journal homepage: www.elsevier.com/locate/jpowsour

Modeling of oxygen reduction mechanism for 3PB and 2PB pathways at solid oxide fuel cell cathode from multi-step charge transfer

Mingyang Gong[a], Randall S. Gemmen[b], Xingbo Liu[a,*]

[a] Department of Mechanical and Aerospace Engineering, West Virginia University, Morgantown, WV 26506, United States
[b] National Energy Technology Laboratory, Morgantown, WV 26507, United States

ARTICLE INFO

Article history:
Received 23 August 2011
Received in revised form 31 October 2011
Accepted 1 November 2011
Available online 7 November 2011

Keywords:
Solid oxide fuel cell
MIEC cathode
Oxygen reduction kinetics
Modeling

ABSTRACT

Oxygen reduction at the mixed ionic and electronic conductive (MIEC) SOFC cathodes occur along a surface pathway with oxygen transport through a triple-phase boundary (3PB), and/or a bulk pathway via bulk cathode and electrolyte/cathode interface (2PB). The identification of the rate-limiting steps (RLSs) for each path and understand on their interactions are important to the SOFC cathode kinetics. In this research a modified one-dimensional continuum model is developed to analyze the oxygen reduction on LSM-type MIEC cathode by incorporating multi-step charge-transfer into the bi-pathway kinetics. Finite control-volume method is used to simulate the pathway kinetic competition, and a parametric study is performed with different equilibrium concentrations of surface oxygen ion ($C_{O^-,eq}$) and bulk oxygen vacancy ($C_{V,MIEC,eq}$). The *I–V* profiles show kinetic transition from 3PB-control to 2PB-control at overpotentials from −0.2 V to −0.4 V, and the active reaction zone in concentration profiles expands from 3PB/2PB interfaces by 2–4 μm. The exchange and local 3PB currents recognized from simulation indicate limit of surface oxygen diffusion as the mechanistic process for pathway transition. The results are compared to the reported experimental findings to examine the model's assumption of oxygen reduction scenario, and its potential implication on SOFC cathode performance improvement.

1. Introduction

For decades, solid oxide fuel cells (SOFCs) have been widely investigated as a promising energy conversion system with advantageous efficiency, fuel flexibility and emissions [1,2]. Yittria-stablized-zirconia (YSZ) is commonly applied as a stable and economical electrolyte material [3,4], while various perovskite oxides with mixed ionic and electronic conductivity (MIEC) are developed into cathode materials. Among them strontium-doped lanthanum manganite (LSM) appears as the conventional choice due to good electrical property, reliability and low-cost [5]. It also serves as a stand-point for understanding of the reaction fundamentals and development of more active cathodes, such as (La,Sr)CoO_3 (LSC) and (La,Sr)(Co,Fe)O_3 (LSCF). It is economically desirable for the SOFC to operate at an intermediate temperature typical of 700–850 °C, but higher electrode performance is then required to overcome the increased ohmic resistance. As a major portion of polarization loss is from relatively sluggish oxygen reduction [6,7], intensive efforts have been devoted to investigate and improve SOFC cathodes kinetics. Even so, questions remain on the assignment of rate-limiting steps (RLSs) to the available kinetic pathways and their expected connection to cathode activation [8,9]. Particularly for the LSM-based cathode, oxygen transport across the cathode/electrolyte interface is known to be restricted by the low intrinsic ionic conductivity of LSM. The reported RLSs accordingly include charge-transfer to the oxygen adsorbate, surface oxygen diffusion, and incorporation of oxygen adsorbate at the triple-phase-boundary (3PB) as suggested by AC impedance and DC polarization study [10–13]. When conditioned by cathodic current, partial reduction of Mn cations and subsequent oxygen vacancy formation in LSM are often suggested as the activation mechanism [14–16], although removal of surface passive species and microstructural change are also considered responsible [17–19]. Nevertheless, debates between chemical versus electrochemical control on the gas-electrode reactions further complicate identification of RLSs and interpretation of activation behaviors [20,21]. In a sense of reducing experimental uncertainty

* Corresponding author. Fax: +1 304 293 6689.
E-mail address: xingbo.liu@mail.wvu.edu (X. Liu).

0378-7753/$ – see front matter © 2011 Elsevier B.V. All rights reserved.
doi:10.1016/j.jpowsour.2011.11.002

Nomenclature

$C_{O^-_{ad}}$ & C_{O^-}	concentration of adsorbed surface oxygen ion
$C_{O^-_{ad},eq}$ & $C_{O^-,eq}$	equilibrium concentration of adsorbed surface oxygen ion
$C_{O^-_{zd},3PB}$	concentration of adsorbed surface oxygen ion at 3PB ($x=0$)
$C_{V,MIEC}$ & C_V	concentration of oxygen vacancy inside MIEC cathode
$C_{V,MIEC,eq}$ & $C_{V,eq}$	equilibrium concentration of oxygen vacancy in cathode
$C_{V,MIEC,x=lc}$	concentration of oxygen vacancy at MIEC/EC boundary ($x=lc$)
$C_{V,YSZ}$	concentration of oxygen vacancy inside YSZ electrolyte
E_{eq}^{WE}	working electrode potential at thermal equilibrium (OCV)
E^{RE}	reference electrode potential
E_{OCV}	open-circuit potential for the cell
E_{2PB}	2PB electrode potential as electrostatic potential difference across 2PB
E_{2PB}^{OC}	2PB electrode potential at OCV
E_{3PB}	3PB electrode potential as electrostatic potential difference across 3PB
E_s	surface electrode potential as electrostatic potential difference across gas/MIEC
Φ^{MIEC}	bulk electrostatic potential of MIEC
$\Phi^{S,MIEC}$	surface electrostatic potential of MIEC
Φ^{YSZ}	bulk electrostatic potential of YSZ
μ_i^{MIEC}	electrochemical potential of species i in MIEC
$\mu_{i,chem}^{MIEC}$	chemical potential of species i in MIEC
μ_i^{YSZ}	electrochemical potential of species i in YSZ
$\mu_{i,chem}^{YSZ}$	chemical potential of species i in YSZ

and fundamental ambiguity, mechanistic approaches merit, either by using patterned micro-electrodes to observe RLSs as functions of well-defined electrode geometric parameters [22–24] or through numerical parametric simulations to study the fundamental kinetics of the reaction pathways and facilitate experimental design.

Presently there are two different pathways recognized for oxygen reduction on an MIEC cathode [25], in which overall oxygen transport occurs through exposed 3PB or the buried cathode/electrolyte boundary (2PB). Concurrent mass and charge transfer proceed as: (i) gaseous diffusion to the electrode surface; (ii) surface oxygen exchange reactions; (iii) surface and bulk solid-state diffusion of oxygen species; and (iv) charge-transfer at the 3PB and 2PB. Fundamental models of the MIEC cathodes have systematically studied kinetic contribution from reaction steps (i)–(iv) to unveil the essential RLSs for oxygen reduction via different mechanisms, however only one single kinetic pathway is usually considered dominant in practice. For study focusing on 2PB-pathway, a continuum model was first proposed by Alder, Lane and Steele to analyze oxygen reduction on *single-phase* MIEC cathode [20], and the model based on chemical kinetics accurately interpreted impedances for highly ionic conductors, but was unconvincing for poor ionic conductors on which 3PB-pathway reaction may dominate. Søgaard then modeled the 2PB-pathway reactions for a *composite* SOFC cathode from similar chemical kinetics assumption with a finite volume method [26]. In contrast, Fleig derived a model for 2PB-pathway kinetics by assuming electrochemical driving force of the surface potential step from a dipole layer of surface oxygen ion [27], and Mebane further developed Fleig's approach into a 2-D model from first principle analysis, which not only compared the importance of the electrochemical driving force versus the chemical one for 2PB-pathway reactions, but also identified geometric charge inhomogeneity [28]. On the other hand for 3PB-pathway, Tanner and Virkar built up both 1-D and 2-D models to quantify microstructural effects on the total 3PB reaction kinetics [29,30].

The results together promote understanding and design of the SOFC cathode; however there are frequent cases that two kinetic pathways may co-exist competitively, especially when a poor-MIEC cathode is can be transformed into MIEC by operation at high overpotential. Takeda and Siebert first used semi-empirical models to summarize kinetic contributions from both pathways for activation of LSM cathode [14,16]. Liu then developed a comprehensive reaction model from the bi-pathway kinetics [31,32]. Svensson proposed a 1-D model to parametrically simulate the bi-pathway kinetics on MIEC cathodes [33,34]. Coffey later improved the model to establish the 3PB-to-2PB pathway transition by quantifying the current–overpotential response [35]. These efforts employ measurable or tabulated material property parameters, and thus guide experimental probe. However, if applying the models on a poor-MIEC cathode for which pathway transition most likely to appear during activation, two challenges may occur. First, the assumptions on chemical driving force for the oxygen-MIEC surface reactions and single-step charge-transfer for interfacial reactions need reconsideration. Experimental study by van Heuveln and other researchers indicated charge-transfer on LSM-type cathode was a multiple-step process [10–12]. Phenomenological and first-principle analysis also suggested surface reactions to be electrochemically driven [27,28,36]. Second as Adler stated [5], simulation of steady-state electrode behavior cannot be used to predict impedance and other transient physical processes.

Inspired by prior works, a one-dimensional diffusion model is developed in this study to simulate the bi-pathway oxygen reduction on a MIEC cathode from multi-step charge-transfer kinetics. This mode would complement Svensson and Coffey's models in the above two aspects mentioned: first we treat the overall oxygen reduction as a multiple-step charge-transfer process, in which not only the 2PB and 3PB interfacial reaction rates, but also the gas/MIEC surface reaction rates are phenomenologically applied with Butler–Volmer type expressions using electrochemical driving forces. Second, this model analyzes the unsteady diffusion equations for MIEC cathode and utilizes a time-discretization solver to reach steady-state. This approach examines the kinetic pathway transition from a more realistic scenario involving multi-step charge transfer and kinetic evolution. A finite control-volume method is used to visualize the transient defect profiles in the electrode as functions of overpotentials and material physical parameters. The assumption of uniform Fermi-level and perfect current collection throughout the cathode might be problematic for the systems with high oxygen vacancy concentration and certain thin-film structure [27,37], therefore this simulation is primarily designed for a LSM-type poor-MIEC during activation. As the model focuses on comparison of oxygen reduction pathways under charge-transfer RLSs, microstructural diffusion effects are less addressed. The simulation results reveal that the nature of the 3PB-to-2PB kinetics transition involves oxygen vacancy evolution and diffusion limit for surface oxygen as 2PB kinetic contribution increases. Effects of surface and bulk material parameters on kinetic pathway transition are also discussed.

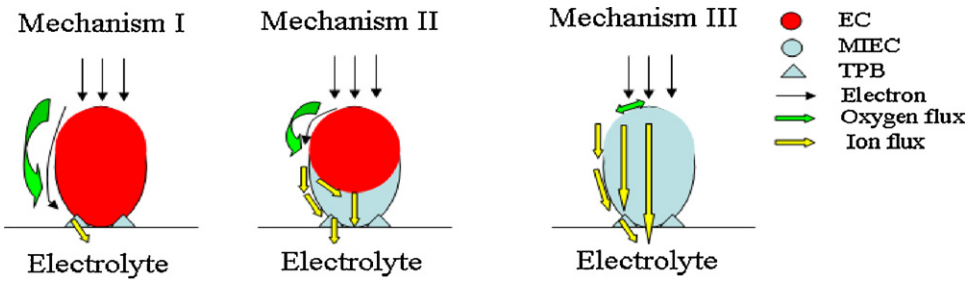

Fig. 1. Three mechanisms for oxygen reduction on SOFC cathode.

2. Physical model

2.1. General schemes for oxygen reduction

Fig. 1 displays the oxygen reduction on a SOFC cathode divided into three mechanisms. Mechanism I depicts materials with poor ionic conductivity and essentially a metallic electronic conductor (EC), which represent LSM-type cathode operated under low overpotential prior to activation. The only active pathway is 3PB charge-transfer. Mechanism III describes a MIEC with good ionic conductivity, which may correspond to LSCF-type cathode with incorporation and diffusion of oxygen adsorbate primarily through the 2PB bulk pathway. The present study interest is mechanism II where electrode kinetics proceeds on two parallel paths. Such a mechanism applies to LSM-type cathode after activation, when the portion of cathode bulk near 3PB/2PB is transformed from EC to MIEC by oxygen vacancy exchange. Oxygen reduction via 2PB pathway then becomes active and complements the existing 3PB pathway kinetics.

2.2. Multi-step charge transfer model

Oxygen transport on an LSM-type cathode in contact with a YSZ electrolyte is described by a 1-D physical model in Fig. 2. The electrode consists of two layers: (1) the MIEC layer (activated portion of LSM with ionic conductivity) next to the 3PB/2PB interface, on which reaction steps (S1–S4, B3–B4) of oxygen adsorption, reduction, and diffusion occur via both 3PB and 2PB paths; (2) an EC outlayer (inactivated portion of LSM) for surface oxygen adsorption (S1). The boundary separating the two layers is defined by where the bulk flux ($J_{\mathrm{diff,V}}$) of oxygen vacancy in the MIEC ($V^{\bullet\bullet}_{\mathrm{O,MIEC}}$) generated via 2PB exchange reaction approaches zero. The only geometric factor is the volume specific surface area of electrode, which is denoted as $\Delta S/\Delta V$ in the model.

The surface (3PB) pathway consists of four elementary steps denoted sequentially as S1–S4, with corresponding physical processes listed in Table 1. The bulk (2PB) pathway shares the first two reaction steps (S1 and S2) with the 3PB pathway, followed by two additional steps of B3 and B4. Adopting Fleig and Mebane's definition [27,28], reaction B3 is derived by breaking the overall surface oxygen/MIEC exchange reaction $O_{ad} + V^{\bullet\bullet}_{\mathrm{O,MIEC}} + 2e \leftrightarrow O^{x}_{\mathrm{O,MIEC}}$ into two half electrochemical reactions S2 and B3. B4 is the net charge-transfer reaction for the 2PB pathway. Above reaction steps are generally set from individual breakdown of the overall 3PB/2PB oxygen reductions, by following previous study on MIEC cathode kinetics [10–13,16,27,28]. Although other kinetic-step scenarios may also merit, the scope of this paper rather tries to provide a numerical treatment method to analyze multi-step charge transfer along different kinetics pathways.

The derivation of reaction rates for each elementary reaction step follows the detailed procedures adopted by van Heuveln, Mebane and Bockris according to the multi-step electrode kinetics and transition-state theory (TST) [10,28,38,39]. The kinetic analysis is based on the fundamentals that for charge-transfer reactions multiple electrons (holes) cannot be transferred simultaneously due to prohibitive activation energy barrier [40].

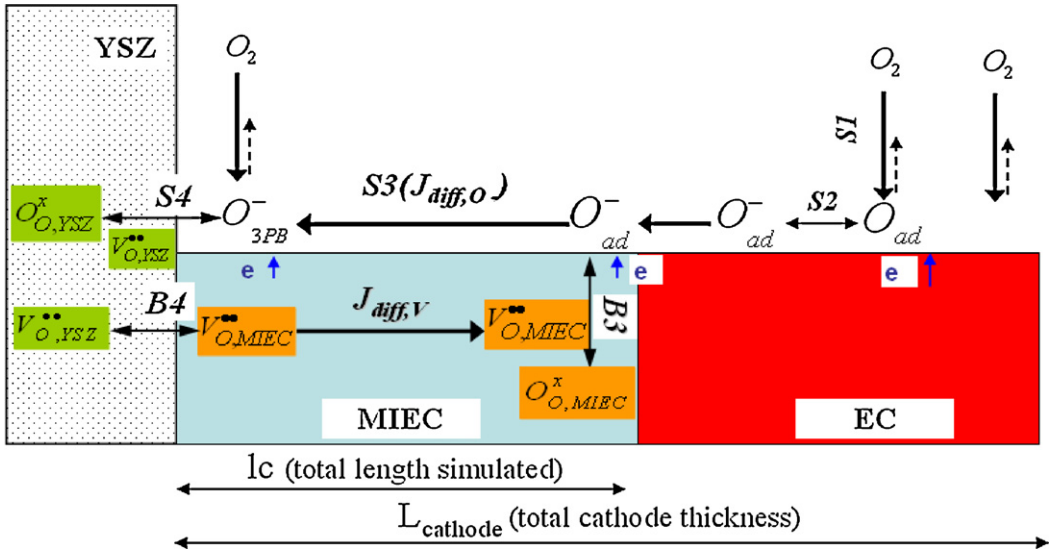

Fig. 2. Schematic description of bi-pathway dominated oxygen reduction on MIEC cathode (LSM).

Table 1
Electrode processes assigned to each elementray steps in surface and bulk pathways.

Pathways	Reaction steps		Process description
Surface	S1	$1/2O_2 + S \underset{k_{S1}^-}{\overset{k_{S1}}{\longleftrightarrow}} O_{ad}$	Dissociate oxygen adsorption (S: surface adsorption site)
	S2	$O_{ad} + e^- \underset{k_{S2}^-}{\overset{k_{S2}}{\longleftrightarrow}} O_{ad}^-$	Oxygen intermediate formation (1st step charge-transfer)
	S3	$O_{ad}^- \underset{k_{S3}^-}{\overset{k_{S3}}{\longleftrightarrow}} O_{TPB}^-$	Surface diffusion towards 3PB
	S4	$O_{TPB}^- + e + V_{O,YSZ}^{\bullet\bullet} \underset{k_{S4}^-}{\overset{k_{S4}}{\longleftrightarrow}} O_O^x$	3PB incorporation of oxygen intermediates (2nd step charge-transfer)
Bulk	B3	$O_{ad}^- + V_{O,MIEC}^{\bullet\bullet} + e^- \underset{k_{B3}^-}{\overset{k_{B3}}{\longleftrightarrow}} O_{O,MIEC}^x$	Reaction of vacancy from MIEC bulk with surface oxygen intermediates
	B4	$O_{O,MIEC}^x + V_{O,YSZ}^{\bullet\bullet} \underset{k_{B4}^-}{\overset{k_{B4}}{\longleftrightarrow}} O_{O,YSZ}^x + V_{O,MIEC}^{\bullet\bullet} + S$	2PB exchange between YSZ and MIEC(S: surface adsorption site)

Generally for a thermal-activated, single-step charge-transfer reaction $OX + e \leftrightarrow RE$, the forward rate constant k_R and backward rate constant k_O are modified by electrostatic potential difference $E_{OX/RE}$ across reaction interface as:

$$k_R = k_R^0 \exp\left(-\frac{\alpha F}{RT} E_{OX/RE}\right) \quad (1)$$

$$k_O = k_O^0 \exp\left(\frac{\alpha F}{RT} E_{OX/RE}\right) \quad (2)$$

where F is the faradic constant, α the symmetry coefficient, R the gas constant and T the reaction temperature; k_R^0 and k_O^0 are collective constant sets with transmission coefficient, Boltzman's constant, standard chemical potentials and activity coefficients as derived by Mebane and Liu [28].

Following this formulism the net rates of the consecutive reaction steps for surface (3PB) and bulk (2PB) pathways can be phenomenologically expressed with species concentrations as:

$$r_{S1} = k_{S1} p_{O_2}^{1/2} \Gamma(1-\theta) - k_{S1}^- \Gamma\theta \quad (3)$$

$$r_{S2} = k_{S2} \Gamma\theta \exp(-\alpha_s f E_s) - k_{S2}^- C_{O_{ad}^-} \exp[(1-\alpha_s) f E_s] \quad (4)$$

$$r_{S3} = k_{S3} C_{O_{ad}^-} - k_{S3}^- C_{O_{zd}^-,3PB} \quad (5)$$

$$r_{S4} = k_{S4} C_{O_{zd}^-,3PB} C_{V,YSZ} \exp(-\alpha_{3PB} f E_{3PB}) - k_{S4}^- \Gamma(1-\theta) \times \exp[(1-\alpha_{3PB}) f E_{3PB}] \quad (6)$$

$$r_{B3} = k_{B3} C_{O_{ad}^-} C_{V,MIEC} \exp(\alpha_s f E_s) - k_{B3}^- \Gamma(1-\theta) \exp[-(1-\alpha_s) f E_s] \quad (7)$$

$$r_{B4} = k_{B4} C_{V,YSZ} \exp(-2\alpha_{2PB} f E_{2PB}) - k_{B4}^- C_{V,MIEC} \times \exp[2(1-\alpha_{2PB}) f E_{2PB}] \quad (8)$$

where k_S, k_S^-, k_B and k_B^- are the forward and backward rate constants for the denoted reaction steps in the two pathways. $C_{O_{ad}^-}$, $C_{V,MIEC}$ and $C_{V,YSZ}$ are the local concentrations for surface oxygen ion, oxygen vacancy inside MIEC cathode and oxygen vacancy of the electrolyte, respectively; Γ is the surface adsorption site density, and θ is the fraction of oxygen site coverage. The symmetry factors, α_{3PB}, α_{2PB} and α_s are taken as 0.5, and thermal factor f is given by $f = F/RT$. Note that although Eq. (5) is written in a way resembling a kinetic reaction for formulism convenience, the process of step S3 is actually surface oxygen diffusion. And the rate constants in Eq. (5) are the same as a ratio of the surface diffusivity over effective surface diffusion distance according to Fick's 1st law [10]. Elementary steps S2, S4 and B3 are simple charge-transfer reactions, while step B4 in Eq. (8) is also a single-step charge-transfer reaction. Following Mebane's practice [28], the electric potential terms E above are the electrostatic potential differences across respective interfaces, with E_s as the surface electrode potential, E_{3PB} the 3PB electrode potential and E_{2PB} the 2PB electrode potential. Detailed definitions and assumptions of these electrode potentials are separately discussed below, and can be further found in Appendix B.

2.3. Potential and overpotential (net driving force) for the reactions

The potential and overpotential of the MIEC electrode is considered in an electrochemical cell with a 3-electrode configuration with the cathode as working electrode (WE), a Pt counter electrode (CE) and a reference electrode (RE). At open circuit, the net reaction rate is zero for the WE. This yields the Nernst relationship between the equilibrium potential of WE and oxygen partial pressure no matter which step is presumably the RLS [10]:

$$E_{eq}^{WE} = \text{constant} + \frac{RT}{4F} \ln p_{O_2}^{WE} \quad (9)$$

The open circuit potential of the cell (E_{OCV}) is the potential difference between the WE and RE, and will only depend on the oxygen activity difference according to Nernst equation [35].

$$E_{OCV} = E_{eq}^{WE} - E^{RE} = -\frac{RT}{4F} \ln p_{O_2}^{RE} + \frac{RT}{4F} \ln p_{O_2}^{WE} \quad (10)$$

Evaluated against an ideal RE, the measured overpotential is due to the change in WE potential:

$$\eta_{tot} = E - E_{OCV} = E^{WE} - E_{eq}^{WE} \quad (11)$$

Next individual electrode potential and overpotential at 3PB, 2PB and cathode surface need to be evaluated. Here distribution of lateral potential and Fermi level is assumed to be uniform for MIEC cathode, which is also taken as reasonable by other 1-D models [34,35]. With this assumption and from the standpoint of good electronic conductivity, surface electrode potential E_s and 3PB electrode potential E_{3PB} are then considered equal to E_{2PB} in Eqs. (4) and (6)–(8). In this model although we follow the Svensson and Coffey's assumptions on electrode potentials in that $E_{3PB} = E_{2PB}$ [33,35], we rather adopt Mebane's method of TST kinetic analysis to define E_{3PB} and E_{2PB} [28], which are the interfacial electrostatic potential differences, as the driving forces for the charge-transfer reactions, because this difference represents activation energy actually driving the reaction. Hence the net driving forces for 3PB and 2PB reactions can be defined as the measured the electrode

overpotentials from OCV, while omitting anode overpotential and cell ohmic potential loss:

$$\eta_{3PB} = E_{3PB} - E_{OCV} \tag{12}$$

$$\eta_{2PB} = E_{2PB} - E_{OCV} \tag{13}$$

which are different from Svensson and Coffey's models as the change of interfacial electrostatic potential differences. Specific derivation of η_{3PB} and η_{2PB} as net driving forces from model assumptions is shown in Appendix B. With $E_{3PB} = E_{2PB}$ assumed for a 1-D model, $\eta_{3PB} = \eta_{2PB}$ can be then derived and the two pathway reactions can have the same net driving force. Similarly, we observe that $\eta_s = \eta_{3PB} = \eta_{2PB}$. It needs to be pointed out that the surface potential change η_s due to charge build-up from oxygen surface exchange can be rather different from the cathode/electrolyte interfacial overpotential, and this could bring about a complicated dependence of η_s on η_{2PB} [27]. This will be further discussed in Section 5, and the present model assumes a simplified relationship between η_s on η_{2PB} for computation convenience. Further discussion on relationship between the electrode potentials and overpotentials can be found in Appendix B.

After separating overpotentials of η_{3PB}, η_{2PB} and η_s from respective electrode potentials, Eqs. (4) and (6)–(8) can be rewritten into Butler–Volmer type expressions [28,39].

$$r_{S2} = r_{S2,0}\left\{\exp(-\alpha_s f\eta_s) - \frac{C_{O^-,ad}}{C_{O^-,ad,eq}}\exp[(1-\alpha_s)f\eta_s]\right\} \tag{14}$$

$$r_{S4} = r_{S4,0}\left\{\frac{C_{O^-_{ad}}}{C_{O^-_{ad},eq}}\exp(-\alpha_{3PB} f\eta_{3PB}) - \exp[(1-\alpha_{3PB})f\eta_{3PB}]\right\} \tag{15}$$

$$r_{B3} = r_{B3,0}\left\{\frac{C_{O^-_{ad}}C_{V,MIEC}}{C_{O^-_{ad},eq}C_{V,MIEC,eq}}\exp(\alpha_s f\eta_s) - \exp[-(1-\alpha_s)f\eta_s]\right\} \tag{16}$$

$$r_{B4} = r_{B4,0}\left[\exp(-2\alpha_{2PB} f\eta_{2PB}) - \frac{C_{V,MIEC}}{C_{V,MIEC,eq}}\exp[2(1-\alpha_{2PB})f\eta_{2PB}]\right] \tag{17}$$

By setting the forward and backward reaction rates equal to each other at OCV, the exchange reaction rates $r_{S2,0}$, $r_{S4,0}$, $r_{B3,0}$ and $r_{B4,0}$ can be derived by replacing E_{OCV} with constants as:

$$r_{S2,0} = k^-_{S2}\left[\frac{k_{S2}k_{S1}\Gamma}{k^-_{S2}k^-_{S1}}p(O_2)^{1/2}\right]^{(1-\alpha_s)}(C_{O^-_{ad},eq})^{\alpha_s} \tag{18}$$

$$r_{S4,0} = k_{S4}\frac{k_{S3}}{k^-_{S3}}\frac{(k_{S4})^{1-\alpha_{3PB}}}{(k^-_{S4}C_{V,YSZ}\Gamma)^{(-\alpha_{3PB})}}(C_{O^-_{ad},eq})^{1-\alpha_{3PB}} \tag{19}$$

$$r_{B3,0} = (k^-_{B3})^{\alpha_s}(k_{B3})^{1-\alpha_s}(\Gamma)^{\alpha_s}(C_{O^-_{ad},eq}C_{V,MIEC,eq})^{1-\alpha_s} \tag{20}$$

$$r_{B4,0} = (k_{B4}C_{V,YSZ})^{1-\alpha_{2PB}}(k^-_{B4}C_{V,MIEC,eq})^{\alpha_{2PB}} \tag{21}$$

3. Formulation of the 1-D numerical model

3.1. Governing equations and boundary conditions

The model considers $C_{O^-_{ad}}$ and $C_{V,MIEC}$ as two independent variables. Concentrations of other species are taken as constant or simple functions of the two primary variables. This condition requires that specific RLSs be screened out for simplifying the calculation requirements and relating the simulation to experimental findings. As for a LSM-type cathode with low intrinsic ionic conductivity, oxygen exchange reactions involving an oxygen vacancy (B3 and B4) can be regarded as rate-limiting. van Heuveln and Jiang's works [10,17] also identified surface electron donation (S2) and oxygen diffusion (S3) as the most possible RLSs for the 3PB kinetics on LSM cathode. For this reason, steps S2, S3, B3 and B4 are set as RLSs with finite net rates, and the steps S1 and S4 remain at quasi-equilibrium with net rates ignored. This scenario highlights contributions of electrochemical reactions to the transition of bi-pathway cathode kinetics in this work, which is the main difference from previous models [33–35]. The coupled mass-transport equations can be built for the two dependent variable species using Fick's 2nd law for diffusion:

$$\begin{aligned}\frac{\partial C_{O^-,ad}}{\partial t} &= D_{s,chem}\left(\frac{\partial^2 C_{O^-,ad}}{\partial x^2}\right) + (r_{S2} - r_{B3}) = D_{s,chem}\left(\frac{\partial^2 C_{O^-,ad}}{\partial x^2}\right)\\ &+ r_{S2,0}\left\{\exp(-\alpha_s f\eta_s) - \frac{C_{O^-,ad}}{C_{O^-,ad,eq}}\exp[(1-\alpha_s)f\eta_s]\right\}\\ &- r_{B3,0}\left\{\frac{C_{O^-_{ad}}C_{V,MIEC}}{C_{O^-_{ad},eq}C_{V,MIEC,eq}}\exp(\alpha_s f\eta_s) - \exp[-(1-\alpha_s)f\eta_s]\right\}\end{aligned} \tag{22}$$

$$\begin{aligned}\frac{\partial C_{V,MIEC}}{\partial t} &= D_{b,chem}\left(\frac{\partial^2 C_{V,MIEC}}{\partial x^2}\right) - \frac{\Delta S}{\Delta V}r_{B3} = D_{b,chem}\left(\frac{\partial^2 C_{V,MIEC}}{\partial x^2}\right)\\ &- \frac{\Delta S}{\Delta V}r_{B3,0}\left\{\frac{C_{O^-,ad}C_{V,MIEC}}{C_{O^-,ad,eq}C_{V,MIEC,eq}}\exp(\alpha_s f\eta_s) - \exp[-(1-\alpha_s)f\eta_s]\right\}\end{aligned} \tag{23}$$

where $D_{s,chem}$ and $D_{b,chem}$ are the surface and bulk chemical diffusivities of oxygen and oxygen vacancy, respectively; and $\Delta S/\Delta V$ is the volume-specific surface area.

At the MIEC/EC boundary (x = lc in Fig. 2), a zero-flux boundary condition is considered for surface oxygen ion as in Eq. (24), while for bulk path a blocking boundary condition is effectively established with Eq. (25) assuming oxygen vacancy concentration at this boundary should be same as that at equilibrium, in accordance to the physical assumptions in Fig. 2:

$$\begin{aligned}\frac{\Delta S}{\Delta V}D_{s,chem}\left(\frac{\partial C_{O^-,ad}}{\partial x}\right)\Big|_{x=lc} &= r_{S2} - r_{B3}\\ &= r_{S2,0}\left\{\exp(-\alpha_s f\eta_s) - \frac{C_{O^-_{ad}}}{C_{O^-_{ad},eq}}\exp[(1-\alpha_s)f\eta_s]\right\}\\ &+ D_{b,chem}\left(\frac{\partial C_{V,MIEC}}{\partial x}\right)\Big|_{x=lc}\end{aligned} \tag{24}$$

$$C_{V,MIEC,x=lc} = C_{V,MIEC,eq} \tag{25}$$

At the MIEC/electrolyte interface (x = 0), with r_{S4} ignored at equilibrium it can be derived that

$$C_{O^-_{ad}} = C_{O^-_{ad},eq}\exp(f\eta_{3PB}) \tag{26}$$

$$\begin{aligned}D_{b,chem}\left(\frac{\partial C_{V,MIEC}}{\partial x}\right)V_{x=0} = -r_{B4} &= r_{B4,0}\left[\frac{C_{V,MIEC}}{C_{V,MIEC,eq}}\exp[2(1-\alpha_{2PB})f\eta_{2PB}]\right.\\ &\left. - \exp(-2\alpha_{2PB}f\eta_{2PB})\right]\end{aligned} \tag{27}$$

Hence, we have a Dirichlet-type boundary condition for the surface oxygen ions arising from a charge-transfer reaction assumed fast-enough at 3PB, and a Neumann-type boundary condition for oxygen vacancies of the MIEC bulk assuming a relatively slow 2PB exchange reaction.

Table 2
Values of type I and II parameters used in the simulation cases.

Parameter		Case 1	Case 2	Case 3	Description
I	$D_{b,chem}$	1×10^{-6} cm^2 s^{-1}	Same (as Case 1)	Same	Surface oxygen diffusivity
	$D_{s,chem}$	1×10^{-6} cm^2 s^{-1}	Same	Same	Bulk vacancy diffusivity
	$C_{V,MIEC,eq}$	1×10^{-8} mol cm^{-3}	1×10^{-8} mol cm^{-3}	1×10^{-7} mol cm^{-3}	Equilibrium vacancy conc. in MIEC
	$C_{O^-_{ad},eq}$	1×10^{-11} mol cm^{-2}	1×10^{-10} mol cm^{-2}	1×10^{-10} mol cm^{-2}	Equilibrium surface oxygen conc.
	$r_{S2,0}$	1×10^{-7} mol cm^{-2} s^{-1}	Same	Same	Exchange rate constant for S2
	$r_{B3,0}$	1×10^{-7} mol cm^{-2} s^{-1}	Same	Same	Exchange rate constant for B3
	$r_{B4,0}$	1×10^{-6} mol cm^{-2} s^{-1}	Same	Same	Exchange rate constant for B4
	$\Delta S(\Delta V)^{-1}$	1×10^{5} cm^{-1}	Same	Same	Volume-specific surface area
II	α_{3PB}, α_{2PB}, α_S	0.5	Same	Same	Symmetry factor
	Γ	10^{-9} mol cm^{-2}	5×10^{-9} mol cm^{-2}	5×10^{-9} mol cm^{-2}	Surface adsorption site density
	θ_{eq}	0.01	0.02	0.02	Equilibrium oxygen coverage
	T	1073 K	Same	Same	Temperature
	pO_2	0.21 atm	Same	Same	Oxygen partial pressure

3.2. Numerical method

Instead of direct evaluation of the steady-state solutions as in previous bi-pathway models, a finite control-volume analysis was adopted together with time-discretization to obtain the transient solution of the variables, thus allowing elucidation of non-stationary electrode kinetics. The modeled distance (10 μm) from the MIEC/electrolyte interface ($x = 0$) to MIEC/EC boundary ($x = lc$) is divided into 40 flux nodes with equal spacing. The locations for node properties (e.g. specie concentration) are offset by 1/2 grid spacing away from the flux nodes following Patankar's method with staggered node matrix [41]. The computational code is implemented with Visual C++ 6.0 software. Overpotentials of +0.1 V to −0.45 V are given as the external input with 50–100 mV intervals between data points. At $t = 0$ computation starts with initialization of surface and bulk species profiles using input boundary conditions, and attains steady-state after a calculation period of 240 nominal time-steps, which actually spans from a few hours to tens of hours according to input values and material parameters. Calculation of the model requires a large number of physical parameters, which are roughly classified into type I and II. Type I are measurable material parameters directly used in governing equations and boundary conditions for simulation. Type II includes material parameters like the defined forward/backward rate constants not directly used in numerical solution, and other thermal and electrochemical condition constants. The parameter values for each case are listed in Table 2. Type I parameter values have been given in previous bi-pathway models except for $C_{O^-_{ad},eq}$ [33,35], but were more suited for simulating MIECs with good ionic conductivity. Re-estimation of the values is thus made from LSM properties established by isotopic oxygen exchange (IOE) and electrical conductivity relaxation (ECR) measurements [42–46]. The parameter values in Table 2 are believed to be within order of magnitude accuracy at best due to the lack of experimental data for the simulated conditions. Details on parameter selection are separately discussed in Appendix A.

4. Results and discussion

The simulation was performed with governing Eqs. (22) and (23), boundary conditions (24)–(27) and Table 2 parameters. The transient profiles for electrode species are given in Section 4.1 to monitor the convergence and efficiency of the model. Steady-state

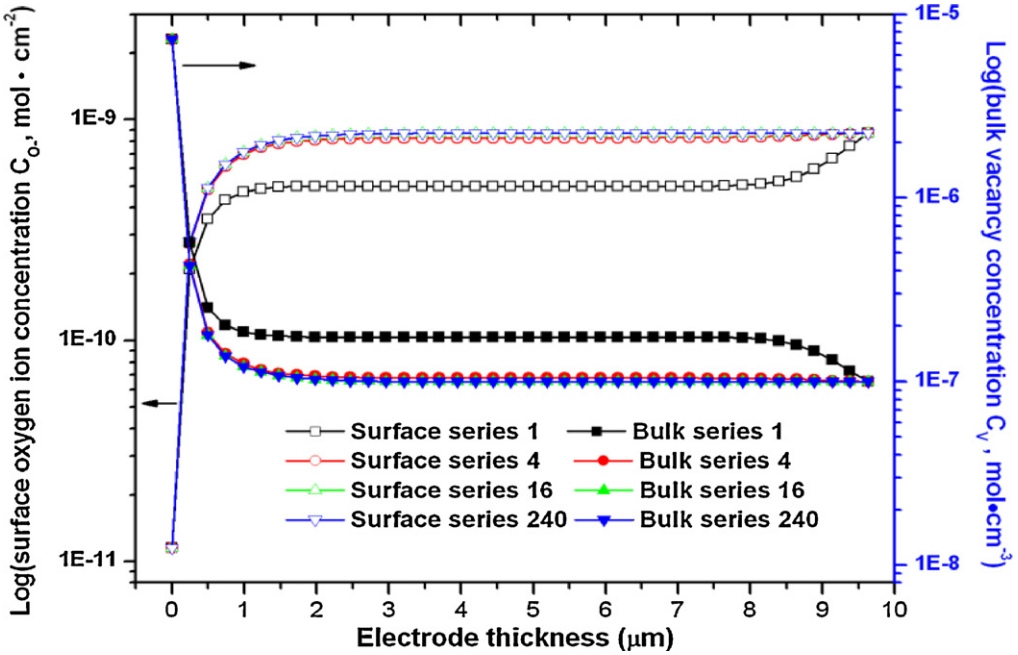

Fig. 3. Transient diffusion profiles of surface oxygen ion and bulk vacancy calculated with $C_{V,eq} = 1 \times 10^{-7}$ mol cm^{-3} and $C_{O^-,eq} = 1 \times 10^{-10}$ mol cm^{-2} at −0.2 V overpotential (open symbol: C_{O^-}; filled symbol: C_V; value of actual time-step: 3.08×10^{-9} s; series 1 = 2.17×10^{-3} s).

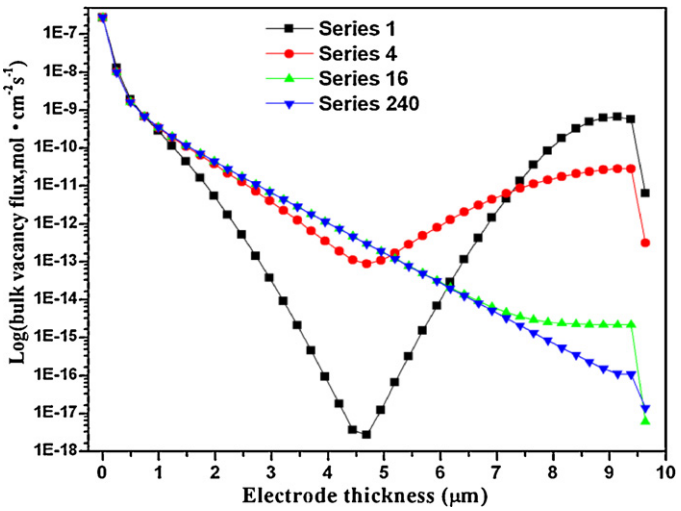

Fig. 4. Transient profiles of the bulk vacancy flux calculated with $C_{V,eq} = 1 \times 10^{-7}$ mol cm^{-3} and $C_{O^-,eq} = 1 \times 10^{-10}$ mol cm^{-2} at −0.2 V overpotential (series 1 = 2.17×10^{-3} s).

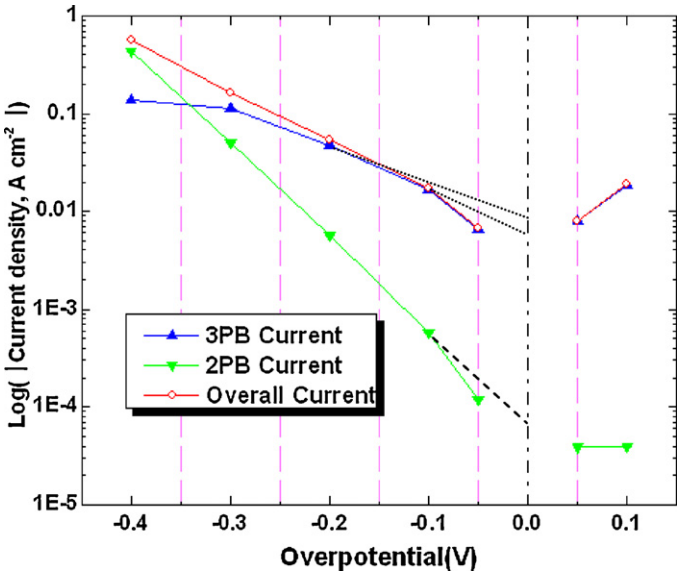

Fig. 5. Logarithmic current versus overpotential profiles for bi-pathway constituted overall electrode kinetics with Case 1 parameters as $C_{O^-,eq} = 1 \times 10^{-11}$ mol cm^{-2} and $C_{V,eq} = 1 \times 10^{-8}$ mol cm^{-3}.

results are discussed in Sections 4.2 and 4.3 to investigate kinetic transition of the MIEC cathode from case to case.

4.1. Transient distribution of the active electrode species

Figs. 3 and 4 show the transient profiles for concentration and diffusion flux of surface oxygen ion (C_{O^-}) and bulk oxygen vacancy (C_V) under moderate overpotential (−0.2 V). Values of $C_{O^-_{ad},eq}$ and $C_{V,MIEC,eq}$ are chosen as those reported for LSM material. A cathodic overpotential of −0.2 V is applied to represent typical SOFC operation condition. Transient-state calculation increases this model's applicability compared to previous steady-state analysis [33–35], as the data can be used to predict AC impedance evolution during electrode activation and also assess the simulation efficiency. The actual time-step used for simulation is about 3×10^{-9} s, which is chosen to meet the stability and plausibility criteria from Patankar [41]. This however, makes convergence slow. To observe how the simulation reaches steady-state, transient profiles are plotted out at certain stages of the actual simulation process, which are denoted as series 1–240 to represent the increment.

Fig. 3 displays surface oxygen concentration distributes in a way reverse to the bulk oxygen vacancy, and their profiles reflect the set-up of reaction rates as boundary conditions at the two interfaces. The species concentrations in Fig. 3 seem to stabilize fast, but Fig. 4 analysis shows the adjustment of the bulk vacancy flux near the MIEC/EC interface lasts until simulation ends. This late convergence at diffusion front of oxygen vacancy spans up to tens of hours. The electrode is further activated at regions adjacent to $x = 0$ (by increase of vacancy flux), and less activated beyond 2–3 μm away from the MIEC/electrolyte interface where 2PB current decays to

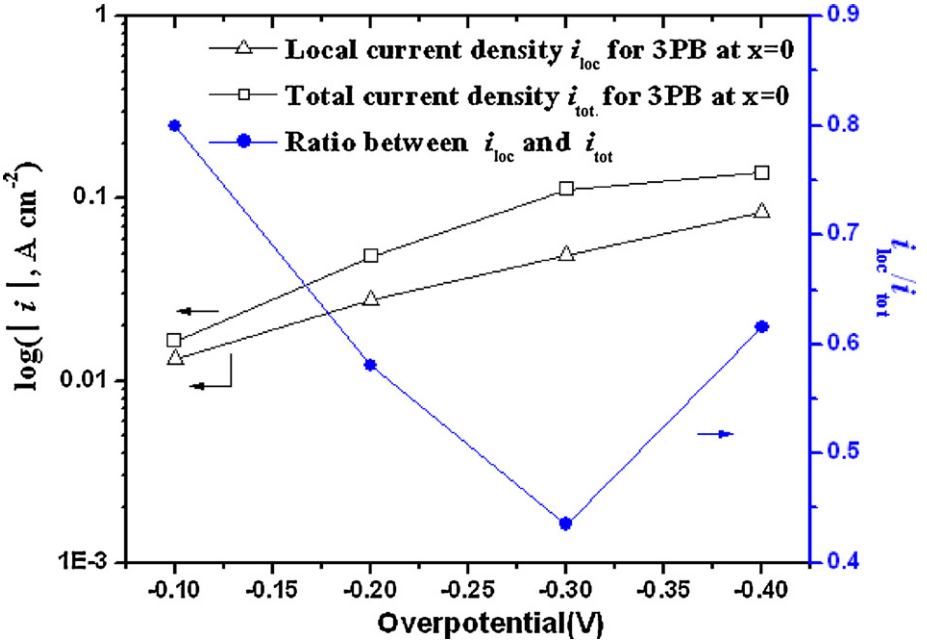

Fig. 6. Evolution of the local reaction current (i_{loc}) in the total 3PB current (i_{tot}) as function of overpotential in Case 1 with $C_{O^-,eq} = 1 \times 10^{-11}$ mol cm^{-2} and $C_{V,eq} = 1 \times 10^{-8}$ mol cm^{-3}.

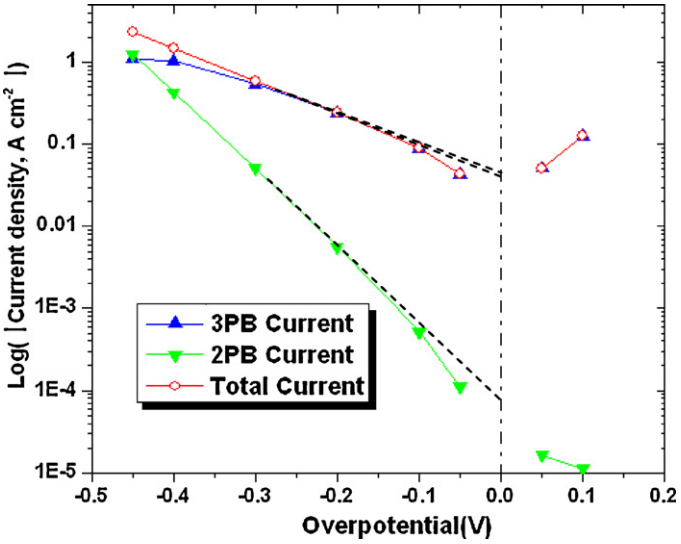

Fig. 7. Logarithmic current versus overpotential profiles with parameters in Case 2 as $C_{O^-,eq} = 1 \times 10^{-10}$ mol cm^{-2} and $C_{V,eq} = 1 \times 10^{-8}$ mol cm^{-3}.

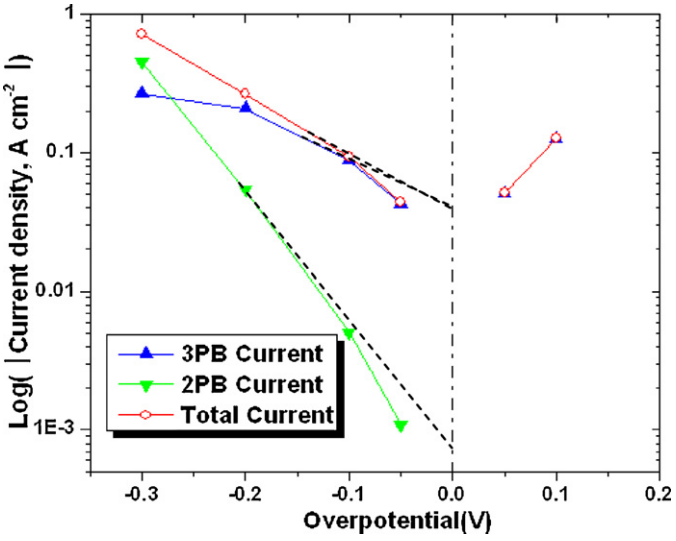

Fig. 8. Logarithmic current versus overpotential profiles with parameters in Case 3 as $C_{O^-,eq} = 1 \times 10^{-10}$ mol cm^{-2} and $C_{V,eq} = 1 \times 10^{-7}$ mol cm^{-3}.

mA range. Analysis on steady-state species distribution and active reaction zone as functions of overpotential and material properties is done in Section 4.3.

4.2. Kinetic transition of the dominant pathway

Relative dominance of the 3PB and 2PB pathways at different overpotentials is investigated to understand how the kinetic transition is affected by material parameters and its consequent impacts on electrode performances. Figs. 5, 7 and 8 are the logarithmic current–overpotential (I–V) curves with separate kinetic pathway contributions for Case 1, 2 and 3, respectively. The simulation is performed between −0.4 V to +0.1 V with 50–100 mV intervals, and the equilibrium concentrations of surface oxygen ion ($C_{O^-,eq}$) and bulk oxygen vacancy ($C_{V,eq}$) are varied among the three cases for a parametric study on electrode kinetics:

(1) $C_{O^-,eq} = 1.0 \times 10^{-11}$ mol cm^{-2} & $C_{V,eq} = 1.0 \times 10^{-8}$ mol cm^{-3} for Case 1
(2) $C_{O^-,eq} = 1.0 \times 10^{-10}$ mol cm^{-2} & $C_{V,eq} = 1.0 \times 10^{-8}$ mol cm^{-3} for Case 2
(3) $C_{O^-,eq} = 1.0 \times 10^{-10}$ mol cm^{-2} & $C_{V,eq} = 1.0 \times 10^{-7}$ mol cm^{-3} for Case 3

Lines are drawn in the figures to display the Tafel estimation of the exchange current densities for the two paths. The exchange current densities, kinetic transition voltage and overall current densities at −0.3 V identified for each case are listed in Table 3. The 3PB and 2PB current densities are given by the fluxes of surface oxygen ions and bulk oxygen vacancies at $x = 0$ respectively as:

$$i_{3PB} = -2F\frac{\Delta S}{\Delta V}D_{s,chem}\left(\frac{\partial C_{O^-,ad}}{\partial x}\right)\Bigg|_{x=0} \quad (28)$$

$$i_{2PB} = 2FD_{b,chem}\left(\frac{\partial C_{V,MIEC}}{\partial x}\right)\Bigg|_{x=0} \quad (29)$$

4.2.1. Overpotential effects on pathway transition

Simulation results from the I–V profiles and corresponding exchange current densities are used to analyze overpotential effects on the kinetic pathway transition for MIEC cathode with Case 1 parameters. With low values of both $C_{O^-,eq}$ and $C_{V,eq}$ in Case 1, Fig. 5 demonstrated that the 3PB pathway dominates at relatively low cathodic and anodic overpotentials, while the 2PB pathway current become increasingly important at higher cathodic overpotentials. A change of dominance on electrode kinetics from 3PB path to 2PB path is observed at around −0.33 V, resulting in a deviation of the total current density from the 3PB current profile and an improved electrode performance. Since this transition of electrode kinetics at negative overpotential is the main research interest, no further simulation in the anodic polarization region (>0.1 V) was made.

The logarithmic relationship between current density and overpotential in Fig. 5 enables a Tafel analysis. Currents from both pathways enter into the Tafel zone at overpotential around −0.1 V, close to value given by high-field approximation of the B–V equation at 800 °C ($-\eta \gg RT/F \approx 0.09$ V) [10,47]. However, the dashed tangent lines of the profiles yield rather different exchange current densities (i_0). For the 3PB pathway, the $i_{0,3PB}$ intercept is about $10^{-2.05}$ A cm^{-2}, matching well with the $i_{S2,0}$ calculated from $r_{S2,0}$ for surface electron donation. Tafel analysis in Fig. 5 finds a rather

Table 3
Summary of V–I curve simulaiton and tafel analysis results for Cases 1–3.

Case	$C_{V,eq}$ (mol cm^{-3})	$C_{O^-,eq}$ (mol cm^{-2})	Transition voltage (V)	Set-up of $i_{0,3PB}$ (mA cm^{-2})	Extracted $i_{0,3PB}$ (mA cm^{-2})	Set-up of $i_{0,2PB}$ (mA cm^{-2})	Extracted $i_{0,2PB}$ (mA cm^{-2})	Extracted $i_{0,TOT}$ (mA cm^{-2})	i_{TOT} at −0.3 V (mA cm^{-2})	Control of electrode activation
1	1×10^{-8}	1×10^{-11}	−0.33	10	10	193	7×10^{-5}	7	163	3PB & 2PB reactions
2	1×10^{-8}	1×10^{-10}	−0.45	10	49	193	8×10^{-5}	45	598	Diffusion
3	1×10^{-7}	1×10^{-10}	−0.26	10	45	193	7×10^{-4}	45	719	Diffusion

small 2PB exchange current density $i_{0,2PB}$ of $10^{-4.17}$ A cm^{-2}, comparing to an input $r_{B4,0}$ equivalent to about 10^{-2} A cm^{-2}. The overall exchange current density is close to $i_{0,3PB}$, around 6–7 mA cm^{-2}. The results indicate that the electrode activation in Case 1 is mainly controlled by local reaction S2 to form intermediate O^-. The large deviation of $i_{0,2PB}$ from the input value implies 2PB kinetics is less favored by factors other than electrochemical force. At lower overpotential, electrochemical terms in Eqs. (14)–(17) are less influential, thus O^- from step S2 and oxygen vacancy from 2PB exchange step B4 could chemically favor a positive direction of step B3 reaction, slowing down the increase of vacancy concentration and flux. Additionally the volume-specific surface area ($\Delta S/\Delta V$) as a geometric factor in Eq. (28) also introduces higher 3PB current. Hence a larger driving force for vacancy exchange is needed from more negative overpotentials, so that the 2PB reaction can outweigh the combined geometry and oxygen incorporation effects to dominate over the 3PB pathway kinetics. As a result of the kinetic transition to slower 2PB kinetics, the total exchange current density exhibits a rather lower value than the 3PB exchange current density in this case.

4.2.2. The mechanism of pathway transition

To further understand the interaction between 3PB and 2PB pathways during electrode activation, the composition of 3PB current is analyzed in terms of diffusion and local reaction currents to unveil the mechanistic process potentially involved in the pathway transition. In Figs. 6 and 9 the change of local current density i_{loc} as a function of overpotential is examined for each case. The total 3PB current density i_{tot} can be viewed as the sum of diffusion current density i_{diff} from the accumulative flux of O^- just outside TPB and local current density i_{loc} from surface reactions r_{S2} and r_{B3} at $x = 0$, and then i_{diff} can be expressed as

$$i_{diff} = i_{3PB,tot} - i_{loc} \tag{30}$$

i_{loc} can be derived from the two RLSs as [10,48]

$$i_{loc} = i_{anodic,loc} - i_{cathodic,loc} = \frac{i_{B3,0}^2 (C_{V,MIEC,x=0}/C_{V,MIEC,eq}) \exp[(2\alpha_s) f\eta_s] \cdot i_{S2,0}\{\exp[(2-\alpha_s) f\eta_s] - \exp(-\alpha_s f\eta_s)\}}{\{i_{S2,0} \exp[(2-\alpha_s) f\eta_s] + i_{B3,0}(C_{V,MIEC,x=0}/C_{V,MIEC,eq}) \exp[(1+\alpha_s) f\eta_s]\} \cdot \{i_{S2,0} \exp(-\alpha_s f\eta_s) + i_{B3,0} \exp[-(1-\alpha_s) f\eta_s]\}}$$
$$+ \frac{i_{S2,0}^2 \cdot i_{B3,0} \exp[2(1-\alpha_s) f\eta_s]\{(C_{V,MIEC,x=0}/C_{V,MIEC,eq}) \exp[(1+\alpha_s) f\eta_s] - \exp[-(1-\alpha_s) f\eta_s]\}}{\{i_{S2,0} \exp[(2-\alpha_s) f\eta_s] + i_{B3,0}(C_{V,MIEC,x=0}/C_{V,MIEC,eq}) \exp[(1+\alpha_s) f\eta_s]\} \cdot \{i_{S2,0} \exp(-\alpha_s f\eta_s) + i_{B3,0} \exp[-(1-\alpha_s) f\eta_s]\}} \tag{31}$$

Case 1 study in Fig. 6 shows that at −0.1 to −0.2 V most of the 3PB current density comes from the local reaction current, confirming that electrode activation is mainly controlled by surface reactions of r_{S2} and r_{B3}. The ratio between i_{loc} and i_{diff} decreases as cathodic overpotential increases, and reaches a minimum just before the 3PB-to-2PB transition at −0.3 to −0.4 V. The increasing contribution from diffusion current at −0.1 to −0.3 V indicates that electrode surface beyond 3PB becomes more active for oxygen reduction during the polarization, and the effective reaction zone is expected to extend accordingly towards the MIEC/EC boundary.

Figs. 5 and 6 suggest by what mechanism the electrode kinetics switch from one dominant pathway to the other. The total 3PB current in Case 1 encounters a diffusion limit associated with surface oxygen flux above −0.3 V, suggested by the increase of i_{loc}/i_{tot}. The coincidence of the diffusion limit for 3PB current with kinetic transition to 2PB dominance implies then that the bulk vacancy concentration increases faster than the production of O^- via r_{S2} outside of the 3PB. Consequently, additional surface oxygen diffusion flux towards 3PB is prevented by local consumption via r_{B3}, e.g. a surface diffusion limit occurs. Meanwhile, local reaction current (triangle in Fig. 6) at 3PB appears to be less limited, and with a linear overpotential-dependence. This is because the concentration of O^- at $x = 0$ is directly defined by the boundary condition, and the driving forces for reactions S2 and B3 are almost certain. In general the analysis on 3PB current composition suggests limitation of surface oxygen diffusion as a potential mechanistic process by which kinetic pathway transition occurs. This transition mechanism, however, has seldom been reported. van Heuveln found no diffusion-limiting current for cathode kinetics governed by surface pathway within −0.3 V overpotential [10], while at more negative overpotential Siebert found impedances typical of mass-transport limiting process during cathode kinetics transition to bulk path dominance [16]. In addition, Coffey's simulation also showed a diffusion-limit for 3PB current after the pathway transition, though no specific process was identified [35]. Comparing with the last results, it is clarified in this model that limiting of surface oxygen diffusion is the physical process behind surface-to-bulk pathway transition.

4.2.3. Effect of material property on pathway transition

Figs. 7 and 8 show the effects from change of material property parameters $C_{O^-,eq}$ and $C_{V,eq}$ on the kinetic pathway transition. In Case 2, where a higher value of $C_{O^-,eq}$ is used while the other parameters remain the same as Case 1, 3PB-to-2PB kinetic transition is postponed more negatively to overpotential around −0.45 V and current above 1 A cm^{-2}. In contrast, Fig. 8 shows that the transition of the dominant pathway occurs at more positive overpotential of around −0.26 V due to the increase of $C_{V,eq}$ by 10 times in Case 3 relative to Case 2. The reasons for such kinetic discrepancy for different cases are explored with Tafel analysis and 3PB current division.

Tafel analysis in Fig. 7 yields $i_{0,3PB}$ of $10^{-1.42}$ A cm^{-2} and $i_{0,2PB}$ of $10^{-4.09}$ A cm^{-2} for Case 2. The overall exchange current density is almost identical to the 3PB one, and is not reduced by sluggish 2PB activation as in Case 1. $i_{0,3PB}$ obtained from Fig. 7 is considerably higher than calculated with input S2 and B3 rate constants. This result may suggest surface reactions of O^- no longer dominate 3PB path kinetics. As indicated by Fig. 9, the local current density estimated with Eqs. (30) and (31) accounts for less than 20% ofthe total 3PB current for Case 2, implying surface oxygen diffusion is now the dominant 3PB step. Due to the change of electrode activation to surface diffusion control at higher $C_{O^-,eq}$, both 3PB kinetics and the overall electrode performance improve compared to Case 1. Increase of $C_{O^-,eq}$ in Case 2 would alter the absolute concentration of O^-, though $C_{O^-}/C_{O^-,eq}$ is unchanged at 3PB for certain overpotential. Consequently this introduces a rather higher level of surface oxygen diffusion flux at 3PB in Fig. 9, and gives rise to a larger overall 3PB current. To overcome the increased suppression effects from 3PB path at high $C_{O^-,eq}$, the oxygen vacancy concentration at 2PB has to rise correspondingly higher, and hence the overpotential for pathway transition grows more negative in Case 2. As for Case 3, the higher $C_{V,eq}$ used in simulation brings about a reduction of the total 3PB current and concomitant rise of i_{loc}/i_{tot} ratio in Fig. 9. Basically, this change reflects increasing contribution from 2PB kinetics with the higher value of $C_{V,eq}$, as both concentration and flux of bulk vacancies would increase accordingly. The 2PB exchange current for Case 3 also increases in Fig. 8 at higher $C_{V,eq}$, resulting in a slightly decreased overall exchange current densities comparing to $i_{0,3PB}$.

Notably, this observation reveals that changes in surface and bulk parameters affect electrode kinetics in different manners. An increase of oxygen vacancy equilibrium concentration promotes

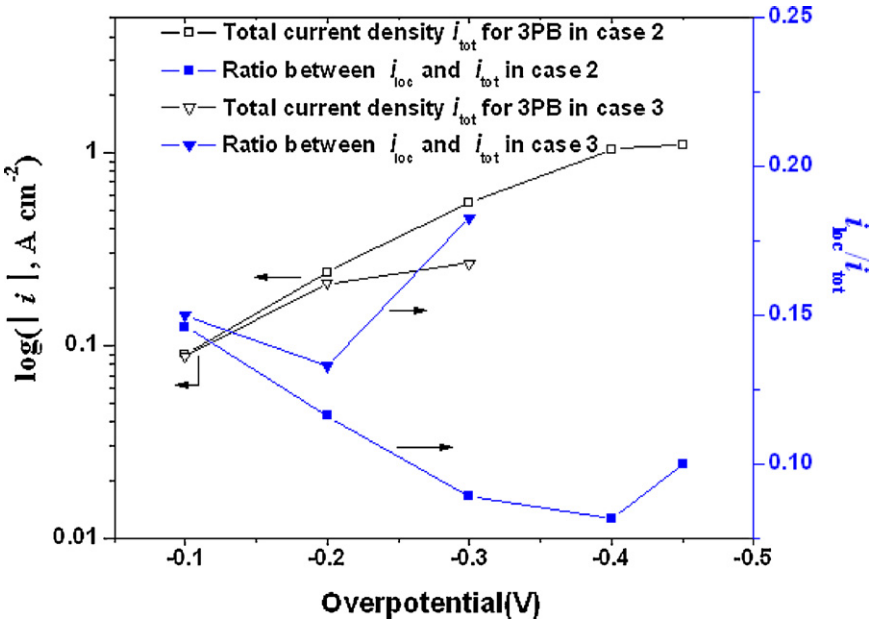

Fig. 9. Comparison of the relationship between local reaction currents and total 3PB currents in Case 2 and Case 3 (Case 2: $C_{O^-,eq} = 1 \times 10^{-10}$ mol cm^{-2} and $C_{V,eq} = 1 \times 10^{-8}$ mol cm^{-3}; Case 3: $C_{O^-,eq} = 1 \times 10^{-10}$ mol cm^{-2} and $C_{V,eq} = 1 \times 10^{-7}$ mol cm^{-3}).

an early transition to bulk pathway and actually limits the oxygen surface diffusion, while large equilibrium coverage of surface oxygen ion improves 3PB kinetics by enhancing oxygen transport on the surface. Despite the differences of electrode kinetics and performance between Cases 1–3, Figs. 6 and 9 did show that the response of i_{loc}/i_{tot} ratio to overpotential follows a similar trend for all the cases studied, confirming the limitation of surface diffusion of oxygen ion as the physical mechanism for 3PB-to-2PB pathway transition.

4.2.4. Association to electrode performance and experimental finding

Combined simulation results from Cases 1–3 indicate that the transition of the dominant pathway greatly depends upon material properties, with earlier transition in terms of cathodic overpotential promoted by decreasing equilibrium surface oxygen concentration $C_{O^-,eq}$ and increasing equilibrium bulk oxygen vacancy concentration $C_{V,eq}$. Change of $C_{O^-,eq}$ and $C_{V,eq}$ also determines the RLS for electrode kinetics, and accordingly the performance in Table 3. From the practical viewpoint, lower overpotential transition of both 2PB and 3PB paths would be preferred to increase total current density. However, from Table 3 it can be learned that earlier 3PB-to-2PB transition does not necessarily lead to higher electrochemical performance. Case 3 has the highest current density at −0.3 V, due to the increased 2PB kinetic contribution at a relatively smaller overpotential. But the dominance of 3PB kinetics in Case 2 leads to greater performance improvement compared to Case 1, even with a late transition voltage. Generally, the value of $C_{O^-,eq}$ can be viewed to associate with electrocatalytic activity of the cathode material, while $C_{V,eq}$ relates to ionic conductivity for the MIEC. For practical development of high performance SOFC cathode, usually poor MIEC like LSM is either directly mixed with a good ionic conductor like YSZ or impregnated with ionic conductive and catalytic active materials, such as doped ceria. The simulation scenario in this study imply that improving surface catalytic activity for a poor MIEC with certain ionic conductivity can be more efficient in terms of electrode performance promotion at a defined electrode configuration (fixed 3PB and 2PB contact area).

In comparison to the simulation results, it is well known for experimental and theoretical studies that SOFC cathode kinetics can be improved at cathodic overpotentials promoting oxygen reduction through bulk pathway. However, the reported overpotential when 2PB contribution becomes apparent tends to vary from case to case. Siebiert noticed considerable current increase for LSM cathodes around overpotential of −0.4 V [16]. Kim reported the resistance of LSM-YSZ electrode was greatly reduced after current treatment at −0.5 V [12]. At higher temperature (950 °C), van Heuveln found significant relaxation of LSM cathode resistance shortly after DC polarization at −0.3 V [10]. More recently, studies from Fleig's group and Shao-Horn's group on dense LSM microelectrodes at 700–800 °C both indicated that the bulk path contribution increased dramatically at DC bias of −300 mV [22,24]. In this work, the simulated overpotential for the pathway transition is around −0.26 V to −0.45 V, lying within the reported data range. The result discrepancy rather reflects that the kinetic transition between surface and bulk path for oxygen reduction is sensitive to electrode operation conditions and material properties, which closely depend on the manufacturing, composition, geometry and structure of the electrode.

4.3. Dependence of active reaction zone and surface reaction rates on overpotential and material parameters

In the physical scenario of oxygen reduction (Fig. 2), a "critical" boundary is assumed to exist at $x = lc$ beyond which surface and bulk exchange reactions would cease to modify the local vacancy concentration from $C_{V,eq}$. The active reaction zone thickness represents the electrode area actually participating in oxygen reduction, and is important to cathode performance improvement through microstructure design. A detailed analysis is thus performed in Sections 4.3.1 and 4.3.2 to derive the thickness of active reaction zone from species concentration profiles and identify its dependence on overpotential and material property from reaction rates r_{S2} and r_{B3}. The results are used to relate simulation findings to the practical routes for cathode performance improvement.

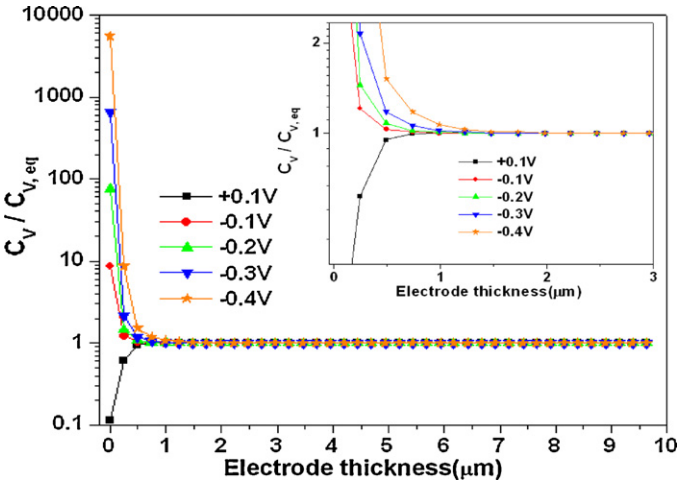

Fig. 10. Distribution profiles of oxygen vacancy concentrations under different overpotential in Case 1 as $C_{O^-,eq} = 1 \times 10^{-11}$ mol cm^{-2} and $C_{V,eq} = 1 \times 10^{-8}$ mol cm^{-3}.

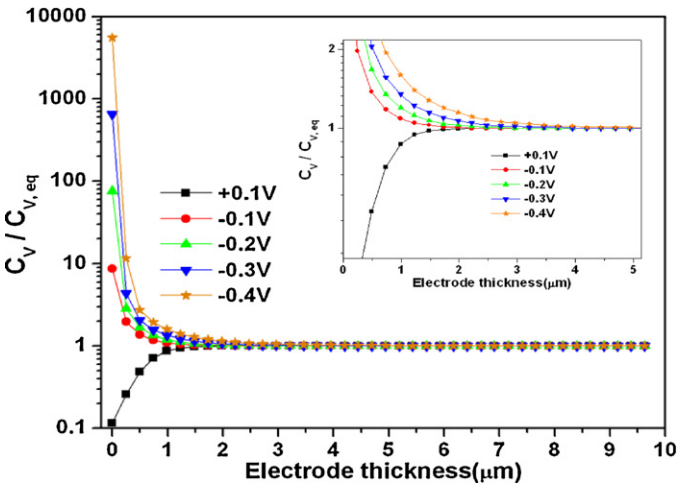

Fig. 11. Distribution profiles of oxygen vacancy concentrations under different overpotential in Case 2 as $C_{O^-,eq} = 1 \times 10^{-10}$ mol cm^{-2} and $C_{V,eq} = 1 \times 10^{-8}$ mol cm^{-3}.

4.3.1. Effects of overpotential and material property on active reaction zone

Figs. 10 and 11 show the overpotential-driven profiles of the normalized oxygen vacancy concentration along the electrode in Case 1 and Case 2, respectively. The electrode is electrochemically activated near 2PB/3PB interfaces as indicated by increased local vacancy concentrations. Applying more negative overpotential increases the penetration depth of oxygen vacancy deviating from thermal equilibrium concentration. In the magnified views of Figs. 10 and 11, the active reaction zone thickness can be seen to extend from ~1 μm in Case 1 to ~4 μm in Case 2 at higher value of $C_{O^-,eq}$. Accordingly, local vacancy concentrations outside of 2PB in Case 2 also increase from Case 1 results. This suggested change of surface material properties not only affects 3PB pathway transport but also the bulk pathway kinetics via a vacancy concentration adjustment. This phenomenon will be addressed in later discussion on methodology for cathode performance improvement. The reason for extension of the active reaction zone is discussed with Fig. 12 results. An increase of $C_{O^-,eq}$ by 10 times in Case 2 relative to Case 1 reduces the local ratio of $C_{O^-}/C_{O^-,eq}$ in Fig. 12 while increasing the surface/bulk exchange reaction rates r_{B3}. It is noteworthy that such changes of $C_{O^-}/C_{O^-,eq}$ ratio and reaction rate r_{B3} are more pronounced at a certain distance away from 3PB, while at 3PB (virtually within one-node distance to it) there is almost no difference of r_{B3} between the two cases. The B3 reaction near $x = 0$ is thus strongly controlled by the boundary condition and relatively independent of material property effects.

Fig. 12 results indicate that the increase of $C_{O^-,eq}$ can reduce $C_{O^-}/C_{O^-,eq}$ while increasing r_{B3}. In Eq. (16), a reduction of $C_{O^-}/C_{O^-,eq}$ and increase of r_{B3} yield larger $C_V/C_{V,eq}$ (e.g. absolute C_V) for a given overpotential. In this way the observed increase of $C_V/C_{V,eq}$ at higher $C_{O^-,eq}$ together with consequent extension of active reaction zone in Fig. 11 can be explained by relative change of $C_{O^-}/C_{O^-,eq}$ and r_{B3} in Fig. 12. An increase of $C_{O^-,eq}$ leads to a higher background chemical potential, and even though absolute concentration of surface oxygen ion rises, the model predicts that the local

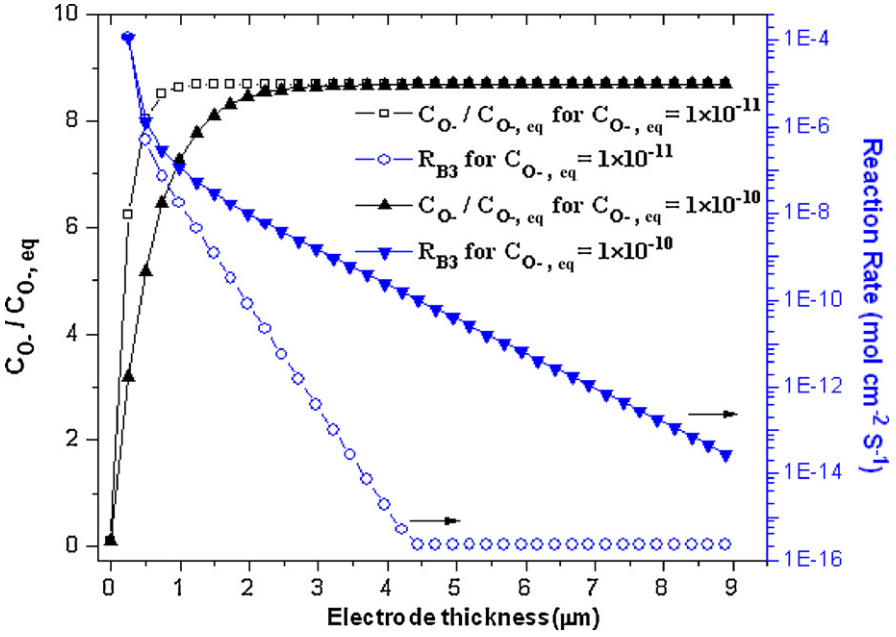

Fig. 12. Distribution profiles of surface oxygen concentrations and step-B3 reaction rates at −0.2 V overpotential in Case 1 and Case 2 as $C_{V,eq} = 1 \times 10^{-8}$ mol cm^{-3}.

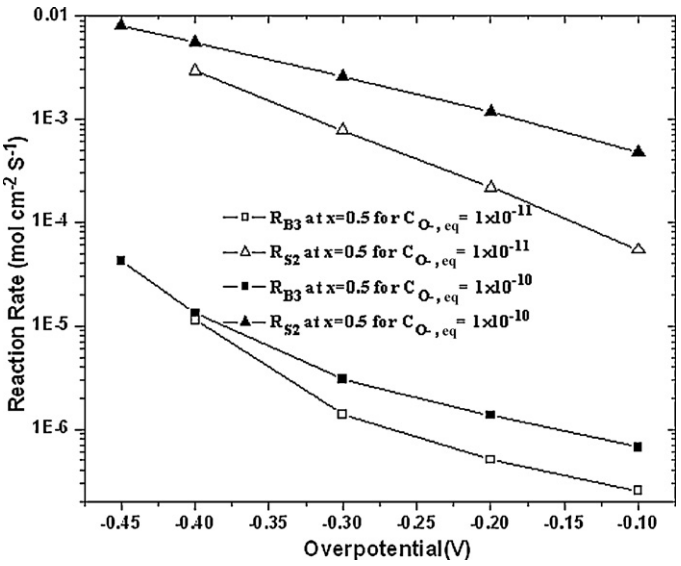

Fig. 13. Dependence of rates of step S2 and B3 reactions at 0.5 μm away from 3PB on overpotential in Case 1 (open symbol) and 2 (filled symbol) as $C_{V,eq} = 1 \times 10^{-8}$ mol cm^{-3}.

chemical potential relating to $C_{O^-}/C_{O^-,eq}$ drops (which is also the case for other cathodic overpotentials; results not shown here). This condition can be expected to slow down reaction B3 according to Eq. (16) initially, and hence promote an increase of local vacancy concentration. Consequently additional vacancy formed via 2PB exchange reaction B4 could be transported to regions away from 2PB until new steady-state level of r_{B3} is achieved. In this way the active reaction zone expands, and electrode kinetics also improve as $C_{O^-,eq}$ increases.

4.3.2. Change of surface reaction rates r_{S2} and r_{B3}

As surface reaction rates r_{S2} and r_{B3} determine local species diffusion fluxes, their profiles as functions of overpotential and $C_{O^-,eq}$ are used to identify reason for occurrence of surface diffusion limit and change of active reaction zone during activation.

In Figs. 12 and 13, r_{B3} outside of 3PB was more positive at negative overpotential, suggesting that the surface reaction is more controlled by the chemical terms $C_V/C_{V,eq}$ and $C_{O^-}/C_{O^-,eq}$ in Eq. (16) than by overpotential. The backward rate in Eq. (16) should increase at more negative overpotential. For r_{B3} to become more positive, $C_V/C_{V,eq}$ and $C_{O^-}/C_{O^-,eq}$ have to increase accordingly to offset the larger backward rate. The magnified comparison in Fig. 14 shows that forward rates of r_{B3} are larger than backward rates at $x = 0.5$ μm. Therefore, step B3 reaction is confirmed to be more "chemically" driven outside of 3PB. However, this result does not necessarily mean that the surface reactions are chemical in nature. Instead r_{S2} remains 2–3 orders of magnitude higher than r_{B3} in Fig. 13. Although combination of reaction S2 and B3 would yield zero charge transfer and hence a chemical oxygen exchange reaction by formulism, the significant rate difference between S2 and B3 reactions makes oxygen intermediates (O^-) a stable phase during reduction, and hence introducing the electrochemical kinetic control [37].

Fig. 13 also shows that at a higher value of $C_{O^-,eq}$, r_{S2} increases faster than r_{B3}, and results in a larger rate difference between r_{S2} and r_{B3} for Case 2 with $C_{O^-,eq} = 1 \times 10^{-10}$ mol cm^{-2}. In the governing equations, the increase of surface diffusion flux can be expected from a larger local rate difference. This explains the change of 3PB pathway kinetics from local reaction control for Case 1 to surface diffusion control for Case 2, as shown by Figs. 6 and 9. It can be also noticed in Fig. 14 that there is an abrupt increase of r_{B3} above the overpotentials for pathway transition, as is shown by slope change of the R_{B3} plots. This indicates that abrupt increase of r_{B3}

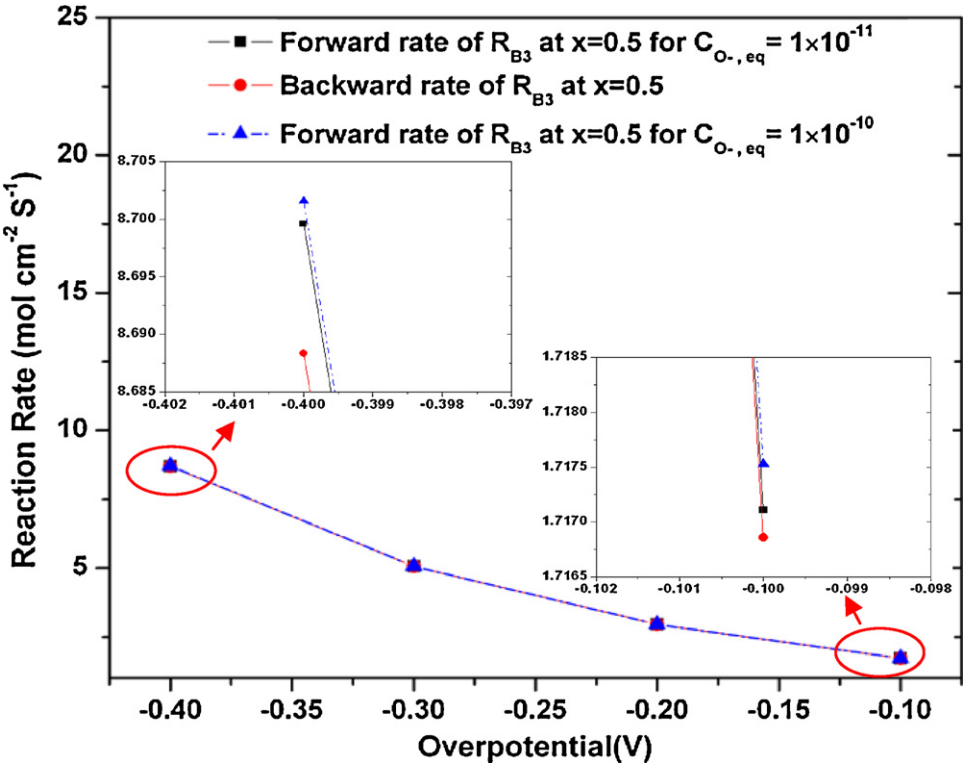

Fig. 14. Dependence of rates of backward and forward reaction rates of step B3 reactions at 0.5 μm away from 3PB on overpotential in Case 1 (open symbol) and 2 (filled symbol) as $C_{V,eq} = 1 \times 10^{-8}$ mol cm^{-3}.

contributes to the limitation of surface diffusion and eventually the 3PB-to-2PB transition.

4.3.3. Association with cathode microstructural design

Together, the above results and discussions are consistent with the assumed existence of an active reaction zone in the MIEC cathode with micron-level thickness. A change in surface material properties affects the 3PB-to-2PB pathway transition by modifying the distribution of surface oxygen ion and bulk vacancy and the corresponding local reaction rates away from the 2PB/3PB interfaces. In comparison, Kuznecov has observed that the diffusion length of oxygen vacancies from the YSZ electrolyte into the LSM cathode was about 2 μm at 950 °C [49], while in general the reported effective oxygen diffusion thickness for LSM derived from oxygen chemical diffusivity (D_{chem}) and surface exchange coefficient (K) ranges from μm to cm-level [42–44]. This large discrepancy may reflect sophisticated control over data acquisition and processing required for thermodynamic property measurement. Simulation in this model does predict a discernible extension of oxygen vacancy diffusion depth, for improved surface catalytic property as a higher $C_{O^-,eq}$ value implies more surface reaction sites available. This finding may offer some guidance on the cathode performance improvement methodology through microstructure design. It is a conventional route to improve kinetics of a poor MIEC cathode through infiltration of ionically conductive second-phase particles such as doped ceria. However, the confined active reaction zone near the electrochemical interfaces in Case 1 implies that impregnated particles need to be in good contact with the 3PB or extended electrolyte network out from the 2PB to effectively affect reaction rates. Thus, control over processing parameters such as precursor viscosity, material loading and sintering temperature would be important to optimize the particle size and distribution. In contrast, the Case 2 study indicates that impregnation with a highly catalytic material could improve surface reaction kinetics and extend the active reaction zone at moderate overpotentials. Hence potentially the second methodology may benefit from less restriction on secondary particle size and distribution to achieve similar performance improvement, since contribution from surface diffusion and reactions outside 3PB becomes more dominant.

5. Model limitation

The oxygen reduction process on the MIEC cathode is broken down into six elementary steps (S1–B4) for the two pathways in this model, and we tentatively propose step S2, B3 and B4 as RLSs based on literature survey and boundary conditions required for numerical solution. Although these are fair assumptions at the given system conditions according to experimental results [10,13,22], there are other possible oxygen reduction scenarios with different elementary steps and RLSs. A recent study on LSM microelectrodes by MIT research group has assigned charge transfer at 2PB/3PB interfaces as RLS below 700 °C and electrode surface reaction as RLS above 700 °C [24]. This finding suggests that there is room for adjustment of the RLS and corresponding boundary conditions at temperatures of interest. Lately, quantum chemistry and first principle analysis show that oxygen adsorption is accompanied by formation of molecular oxygen ions at the electrode surface (O_2^- and O_2^{2-}), which can be subsequently converted into O^- [28,36]. This prediction would complicate RLS assignments and governing equations derivation by introducing additional elementary steps. Another important factor that needs to be taken into consideration for future improvement is, as pointed out by Fleig and Mebane [27,28], that the change of surface potential across the gas/MIEC interface may in general deviate from the nominal bulk overpotential across MIEC/electrolyte interface. Thus, it would be necessary to decouple overpotential driving surface reactions from that driving bulk vacancy exchange. Fleig's study showed that surface overpotential would either linearly depend on the bulk overpotential or remain constant with the range between 0 and 2η (η: bulk overpotential) [27]. In this model, surface overpotential is assumed to be equal to bulk overpotential for computational simplification. To overcome this complexity, a detailed relationship between surface/bulk overpotentials has to be derived with corresponding RLS assumptions of surface reactions.

6. Conclusion and future work

In this study multi-step charge transfer is incorporated into a multi-domain 1-D physical model designed for the oxygen reduction scenario to examine the competitive behaviors between the paralleled 3PB and 2PB kinetic pathway during MIEC electrode activation. Analysis by V–I polarization curve, Tafel estimation and local 3PB current constitution has identified the limitation of surface oxygen ion diffusion as the mechanism for 3PB-to-2PB kinetic transition. The transition voltage between −0.2 and −0.4 V depends on both material surface and bulk parameters. The transition voltage becomes more negative at higher $C_{O^-,eq}$ and less negative at higher $C_{V,eq}$. The model also demonstrated surface reactions are driven predominantly by electrochemical forces at the 3PB, while being controlled by oxygen vacancy concentration variation at regions away from 3PB. Consequently, improving of material surface catalytic activity can effectively promote electrode performance by extending the active reaction zone outside of the 3PB/2PB interface, and may be more efficient than addition of a separate ionic conductor into the electrode via methods such as infiltration. Future development of the model should include: (1) adoption of a physically more plausible oxygen adsorption scenario into 1-D model involving peroxide and superoxide ions; (2) incorporate into the governing reaction mechanisms the interrelationship between surface potential change and bulk overpotential derived from specific assumptions on the surface charging layer configuration; (3) derive cathode impedance from transient simulation results with defined system properties of material, temperature and oxygen partial pressure.

Acknowledgements

The research is sponsored by NETL's URS program and U.S. Department of Energy's EPSCoR program under grant number DE-FG02-06ER46299. The authors thank Dr. Kirk Gerdes and Dr. David S. Mebane from National Energy Technology Laboratory together with Dr. Harry O. Finklea from Department of Chemistry in West Virginia University, for their critical discussions and suggestions during model construction and analysis.

Appendix A. Parameter estimation

Oxygen vacancy diffusivity D_v, which is $D_{b,chem}$ in this model, is reported by Mizusaki to be almost independent of perovskite compositions and vacancy concentrations at 700–1000 °C [50]. Yasuda found that D_v for $La_{0.8}Sr_{0.2}MnO_3$ (LSM20) with values of 10^{-6}–10^{-5} cm^{-2} s^{-1} at 850 °C varied little with oxygen partial pressure (pO_2)[44]. Thus $D_{b,chem}$ is set as 1×10^{-6} cm^{-2} s^{-1} for LSM at 800 °C. Diffusivity of surface oxygen ion $D_{s,chem}$ is kept the same as $D_{b,chem}$ [33,35]. Oxygen vacancy concentration, which is sensitive to material composition, pO_2 and temperature, is estimated by oxygen tracer diffusivity D_O^* [42,46]:

$$D_O^* = fD_V[V_O^{\bullet\bullet}] \quad \text{(A1)}$$

where the correlation factor f is taken as 0.69 for perovskite-type crystal. D_O^* reported for LSM20 at 800 °C ranges from 4×10^{-15} to 1×10^{-13} for pO_2 between 0.13 and 1 atm [42–45]. Substitution of D_V and D_O^* into Eq. (A1) gives vacancy concentration of 5.8×10^{-9} to 1.4×10^{-7}. Thus $C_{V,MIEC,eq}$ is chosen as 1×10^{-8} to 1×10^{-7} mol cm^{-3}, close to Yasuda's value for LSM20 at 900 °C [45]. Literature data are rare for the equilibrium concentration of surface oxygen ion, but this value can be estimated from the equilibrium oxygen coverage and surface adsorption site density as $\Gamma\theta_{eq}$. Γ is reported to be 10^{-8}–10^{-9} mol cm^{-2} for oxygen adsorption and θ_{eq} is usually assumed to be 0.01–0.1 [34,49]. So $C_{O_{ad}^-,eq}$ is set as 1×10^{-10} to 1×10^{-11} mol cm^{-2}. Volume-specific surface area depends on average particle size of the electrode according to close-packaging model [51]:

$$\frac{\Delta S}{\Delta V} = \frac{6}{d_{avg}}(1-\varepsilon) \tag{A2}$$

where d_{avg} is the average particle size, and ε is 0.26 for face-centered cubic lattice. Then $\Delta S/\Delta V = 8.9\times10^6$ m^{-1} if $d_{avg} = 0.5$ μm. So $\Delta S/\Delta V$ is set as 1×10^5 cm^{-1} for submicron-sized particles.

The exchange reaction rates $r_{S2,0}$, $r_{B3,0}$ and $r_{B4,0}$ directly relate to the exchange current densities. AC impedance and DC polarization tests are frequently used to determine i_0 for the specific RLS, however the reported values vary due to different testing conditions and disagreement on kinetic interpretation. van Heuveln obtained i_0 of 20–110 mA cm^{-2} at 950 °C for a LSM electrode with surface electron donation and surface oxygen diffusion as RLSs [10]. While the same RLSs were also assigned by S. Wang on LSM, i_0 was set as 10 mA cm^{-2} at 900 °C [13]. Chen's fitting of i_0 yielded 1–10 mA cm^{-2} for LSM under much lower oxygen partial pressure at 800 °C [48]. At even lower temperature of 700 °C Horita still obtained an i_0 of 2 mA cm^{-2} for a LSM mesh electrode on YSZ [23]. The value of $r_{S2,0}$ selected in this model gives i_0 around 10 mA cm^{-2}. Estimation of $r_{B3,0}$ and $r_{B4,0}$ is difficult due to lack of data for a LSM electrode. The corresponding rates in Svensson and Coffey's models convert to i_0 well below 1 mA cm^{-2} [34,35]. Such a low value means that the enhancement of electrode kinetics from 2PB pathway may be rather limited. However, if LSM does become a good MIEC like LSF and LSC as expected at higher overpotential, it should exhibit similar kinetic properties for oxygen reduction as these materials. The exchange current densities assigned for LSC and LSCF are generally between 330 and 1100 mA cm^{-2} at 800 °C [52,53]. Hence, $r_{B3,0}$ is set equal to $r_{S2,0}$ considering that surface exchange coefficiency of LSM is about 1–2 orders lower than other good MIECs, and essentially 3PB and 2PB pathways would be competitive on surface reactions. The value of $r_{B4,0}$ is chosen so that $i_{B4,0}$ equal to 193 mA cm^{-2}, indicating step B4 can be RLS at more negative overpotential.

Appendix B. Potential derivation

In Svensson and Coffey's models, the driving force for 2PB and 3PB reactions are defined as the electrochemical potential difference between the involved reaction species across the interface, which for 2PB reaction can be expressed as [34,35]:

$$2F\eta_{2PB}^S = \mu_{\nu,2PB}^{MIEC} - \mu_{\nu,2PB}^{YSZ} \tag{B1}$$

where η_{2PB}^S is the defined driving force for 2PB reaction, and $\mu_{\nu,2PB}^{MIEC}$ and $\mu_{\nu,2PB}^{YSZ}$ are the electrochemical potentials of oxygen vacancy in MIEC cathode and electrolyte, respectively. Then the measured total potential drop between WE and RE in the 3-electrode system is defined in the models from 2PB potential deviation from OCV as [34,35]:

$$E_{2PB} = E_{2PB}^{OC} - \frac{RT}{2F}\ln\frac{C_{\nu,2PB}^{MIEC}}{C_{\nu,2PB}^{oc,MIEC}} + \frac{1}{2F}(\mu_{\nu,2PB}^{MIEC} - \mu_{\nu,2PB}^{YSZ}) \tag{B2}$$

where $C_{\nu,2PB}^{oc,MIEC}$ and $C_{\nu,2PB}^{MIEC}$ are the 2PB oxygen vacancy concentration in MIEC cathode at OCV and polarization, respectively. For a 1-D model assuming uniform lateral potential distribution, the measured 3PB and 2PB potentials must be the same, which is also the case at OCV, hence [35]:

$$E_{2PB} = E_{3PB}, \quad E_{2PB} - E_{2PB}^{OC} = E_{3PB} - E_{3PB}^{OC} \tag{B3}$$

In our model, we define this measured potential difference from OCV as the "net" driving forces for both 3PB and 2PB reactions, therefore we have:

$$\eta_{2PB} = \eta_{3PB} \tag{B4}$$

The physical implication of this overpotential definition is the deviation of the electrostatic potential difference across the interfaces from OCV. With the assumption of dilute solution, the electrochemical potentials for charged species in Eq. (B2) can be expressed as [34]:

$$\mu_{\nu,2PB}^{MIEC} = \mu_\nu^0 + RT\ln C_{\nu,2PB}^{MIEC} + 2F\Phi_{2PB}^{MIEC} = \mu_{\nu,chem,2PB}^{MIEC} + 2F\Phi_{2PB}^{MIEC} \tag{B5}$$

$$\mu_{\nu,2PB}^{YSZ} = \mu_\nu^0 + RT\ln C_{\nu,2PB}^{YSZ} + 2F\Phi_{2PB}^{YSZ} = \mu_{\nu,chem,2PB}^{YSZ} + 2F\Phi_{2PB}^{YSZ} \tag{B6}$$

where μ_ν^0 is the stand reference state, Φ the electrostatic potential and $\mu_{\nu,chem}$ the chemical potential of oxygen vacancy at 2PB. Substitute Eqs. (B5) and (B6) into Eq. (B2), it can written that

$$E_{2PB} = E_{2PB}^{OC} - \frac{RT}{2F}\ln\frac{C_{\nu,2PB}^{MIEC}}{C_{\nu,2PB}^{oc,MIEC}} + \frac{1}{2F}(\mu_{\nu,chem,2PB}^{MIEC} - \mu_{\nu,chem,2PB}^{YSZ}) + \Phi_{2PB}^{MIEC} - \Phi_{2PB}^{YSZ} \tag{B7}$$

At OCV we know that $\mu_{\nu,2PB}^{oc,MIEC} = \mu_{\nu,2PB}^{oc,YSZ}$, which leads to

$$\mu_{\nu,chem,2PB}^{oc,MIEC} + 2F(\Phi_{2PB}^{oc,MIEC} - \Phi_{2PB}^{oc,YSZ}) = \mu_{\nu,chem,2PB}^{oc,YSZ} \tag{B8}$$

And if vacancy concentration in electrolyte is assumed to keep constant during reaction, then we get $\mu_{\nu,chem,2PB}^{YSZ} = \mu_{\nu,chem,2PB}^{oc,YSZ}$. So Eq. (B8) can be substituted into Eq. (B7) to get

$$E_{2PB} = E_{2PB}^{OC} - \frac{RT}{2F}\ln\frac{C_{\nu,2PB}^{MIEC}}{C_{\nu,2PB}^{OC,MIEC}} + \frac{1}{2F}(\mu_{\nu,chem,2PB}^{MIEC} - \mu_{\nu,chem,2PB}^{oc,MIEC}) + (\Phi_{2PB}^{MIEC} - \Phi_{2PB}^{YSZ}) - (\Phi_{2PB}^{oc,MIEC} - \Phi_{2PB}^{oc,YSZ}) \tag{B9}$$

Therefore, by eliminating the vacancy concentration terms from Eq. (B9) we obtain

$$\eta_{2PB} = E_{2PB} - E_{2PB}^{OC} = (\Phi_{2PB}^{MIEC} - \Phi_{2PB}^{YSZ}) - (\Phi_{2PB}^{oc,MIEC} - \Phi_{2PB}^{oc,YSZ}) \tag{B10}$$

With introduction of surface oxygen intermediate ion O^-, we can also derive the modified driving forces for the 3PB reaction as:

$$\eta_{3PB} = (\Phi_{3PB}^{MIEC} + \Phi_{3PB}^{S,MIEC} - 2\Phi_{3PB}^{YSZ}) - (\Phi_{3PB}^{oc,MIEC} + \Phi_{3PB}^{oc,S,MIEC} - 2\Phi_{3PB}^{oc,YSZ}) \tag{B11}$$

where $\Phi_{3PB}^{S,MIEC}$ is the surface electrostatic potential of MIEC at 3PB. If zero electrical field is assumed between 3PB and 2PB interfaces, then we have

$$\Phi_{3PB}^{MIEC} = \Phi_{2PB}^{MIEC}, \quad \Phi_{3PB}^{YSZ} = \Phi_{2PB}^{YSZ} \tag{B12}$$

The derivation of $\eta_{2PB} = \eta_{3PB}$ would imply $\Phi_{3PB}^{S,MIEC} = \Phi_{3PB}^{YSZ}$, which indicates that at triple-phase-boundary where the MIEC cathode surface emerges with electrolyte, its electrostatic potential would assume the same value as that of electrolyte surface. With similar definition from Eqs. (B10) and (B11), we can obtain the surface overpotential η_s as

$$\eta_s = E_s - E_s^{OC} = (\Phi^{MIEC} - \Phi^{S,MIEC}) - (\Phi^{oc,MIEC} - \Phi^{oc,S,MIEC}) \quad \text{(B13)}$$

where surface electrode potential E_s is difference between the bulk electrostatic potential of MIEC Φ^{MIEC} and the surface electrostatic potential of MIEC $\Phi^{S,MIEC}$. The change of electrostatic potential difference in Eqs. (B10), (B11) and (B13) as net driving forces for electrochemical reactions can then be used to obtain B–V kinetic Eqs. (14)–(17) through transition-state-theory analysis in Mebane's model [28]. As discussed in Sections 2.3 and 5 the model assumed a simplified relationship between surface potential step and interfacial overpotentials, out from zero electrical field assumption inside the MIEC bulk and on its surface. For a poor ionic MIEC like LSM, its bulk background charge would be 5–6 orders of that carried by oxygen vacancy with initial comparison of this study to Mebane and Svensson's models [34,37]. For the simulated overpotential range in this model, the increase of bulk charge due to vacancy exchange into MIEC can be estimated to be around 1% at most. Therefore as estimated by Svensson et al. [34], the species migration flux in this case can be negligible to the diffusion flux. However, the model can break down for simulation of good ionic MIEC with much higher intrinsic oxygen vacancy concentration. And then a modified model with independent consideration of surface potential and electrical field effects would be required.

References

[1] N.Q. Minh, T. Takahashi, Science and Technology of Ceramic Fuel Cells, Elsevier, Amsterdam, 1995.
[2] M.C. Williams, J.P. Strakey, W.A. Surdoval, Int. J. Appl. Ceram. Technol. 2 (2005) 295–300.
[3] S.P.S. Badwal, Solid State Ionics 143 (2001) 39–46.
[4] K.C. Wincewicz, J.S. Cooper, J. Power Sources 140 (2005) 280–296.
[5] S.B. Adler, Chem. Rev. 104 (2004) 4791–4843.
[6] E. Ivers-Tiffée, A. Weber, D. Herbstritt, J. Eur. Ceram. Soc. 21 (2001) 1805–1811.
[7] Y. Jiang, A.V. Virkar, F. Zhang, J. Electrochem. Soc. 148 (10) (2001) A1091–A1099.
[8] J. Fleg, Annu. Rev. Mater. Res. 33 (2003) 361–382.
[9] S.B. Adler, J. Electrochem. Soc. 149 (2002) E166–E172.
[10] F.H. van Heuveln, H.J.M. Bouwmeester, J. Electrochem. Soc. 144 (1997) 134–140.
[11] X.J. Chen, K.A. Khor, S.H. Chan, J. Power Sources 123 (2003) 17–25.
[12] J.-D. Kim, G.-D. Kim, J.-W. Moon, Y.-I. Park, W.-H. Lee, K. Kobayashi, M. Nagai, C.-E. Kim, Solid State Ionics 143 (2001) 379–389.
[13] S. Wang, X. Lu, M. Liu, J. Solid State Electrochem. 6 (2002) 384–390.
[14] Y. Takeda, R. Kanno, M. Noda, Y. Tomida, O. Yamamoto, J. Electrochem. Soc. 134 (11) (1987) 2656–2661.
[15] Y. Jiang, S. Wang, Y. Zhang, J. Yan, W. Li, J. Electrochem. Soc 145 (1998) 373–378.
[16] E. Siebert, A. Hammouche, M. Kleitz, Electrochim. Acta 40 (11) (1995) 1741–1753.
[17] S.P. Jiang, J.G. Love, Solid State Ionics 138 (2001) 183.
[18] X.J. Chen, K.A. Khor, S.H. Chan, Solid State Ionics 167 (2004) 379–387.
[19] M. Kuznecov, P. Otschik, P. Obenaus, K. Eichler, W. Schaffrath, Solid State Ionics 157 (2003) 371–378.
[20] S.B. Adler, J.A. Lane, B.C.H. Steele, J. Electrochem. Soc. 143 (11) (1996) 3554–3564.
[21] M. Liu, J. Winnick, Solid State Ionics 118 (1999) 11–21.
[22] V. Brichzin, J. Fleig, H.-U. Habermeier, G. Cristiani, J. Maier, Solid State Ionics 152–153 (2002) 499–507.
[23] T. Horita, K. Yamaji, N. Sakai, Y. Xiong, T. Kato, H. Yokokawa, T. Kawada, J. Power Sources 106 (2002) 224–230.
[24] G.J. la O', B. Yildiz, S. McEuen, Y. Shao-Horn, J. Electrochem. Soc. 154 (2007) B427–B438.
[25] J. Fleig, J. Power Sources 105 (2002) 228–238.
[26] M. Søgaard, P.V. Hendriksen, T. Jacobsen, M. Mogensen, Proceedings of the 7th European SOFC Forum European Fuel Cells Group, Lucerne, Switzerland, July, 2006.
[27] J. Fleig, Phys. Chem. Chem. Phys. 7 (2005) 2027–2037.
[28] D.S. Mebane, M. Liu, J. Solid State Electrochem. 10 (2006) 575–580.
[29] C.W. Tanner, K.-Z. Fung, A.V. Virkar, J. Electrochem. Soc. 144 (1997) 21–30.
[30] A.V. Virkar, J. Chen, C.W. Tanner, J.W. Kim, Solid State Ionics 131 (2000) 189.
[31] M. Liu, J. Winnick, J. Electrochem. Soc. 144 (1997) 1881–1884.
[32] M. Liu, J. Electrochem. Soc. 145 (1) (1998) 142–154.
[33] A.M. Svensson, S. Sunde, K. Nisancioglu, J. Electrochem. Soc. 144 (1997) 2719–2732.
[34] A.M. Svensson, S. Sunde, K. Nisancioglu, J. Electrochem. Soc. 145 (1998) 1390–1400.
[35] G.W. Coffey, L.R. Pederson, P.C. Rieke, J. Electrochem. Soc. 150 (8) (2003) A1139–A1151.
[36] Y.M. Choi, D.S. Mebane, J.-H. Wang, M. Liu, Top. Catal. 46 (2007) 386–401.
[37] D.S. Mebane, Y. Liu, M. Liu, J. Electrochem. Soc. 154 (2007) A421–A426.
[38] J.O'M. Bockris, A. Reddy, Modern Electrochemistry, vol. 2, Plenum Press, New York, 1977.
[39] H.R. Thirsk, J.A. Harrison, A Guide to the Study of Electrode Kinetics, Academic Press, London and New York, 1972.
[40] M. Boudart, Kinetics of Chemical Processes, Prentice-Hall Inc., Englewood-Cliffs, NJ, 1968.
[41] S.V. Patankar, in: W.J. Winkowycz, E.M. Sparrow (Eds.), Numerical Heat Transfer and Fluid Flow, Series in Computational Methods in Mechanics and Thermal Sciences, McGraw-Hill Book Company, New York, 1980.
[42] R.A. De Souza, J.A. Kilner, J.F. Walker, Mater. Lett. 43 (2000) 43–52.
[43] L. Mikkelsen, E. Skou, J. Therm. Anal. Calorim. 64 (2001) 873–878.
[44] I. Yasuda, M. Hishinuma, J. Solid Sate Chem. 123 (1996) 382–390.
[45] I. Yasuda, K. Ogasawaraa, M. Hishinuma, T. Kawada, M. Dokiya, Solid State Ionics 143 (2001) 39–46.
[46] T. Horita, K. Yamaji, N. Sakai, H. Yokokawa, T. Kato, J. Electrochem. Soc. 148 (2001) J25–J30.
[47] A.C. Co, X.J. Xia, V.I. Birss, J. Electrochem. Soc. 152 (3) (2005) A570–A576.
[48] X.J. Chen, K.A. Khor, S.H. Chan, Electrochim. Acta 49 (2004) 1851–1861.
[49] M. Kuznecov, P. Otschik, N. Trofimenko, K. Eichler, Russ. J. Electrochem. 40 (2004) 1355–1363.
[50] J. Mizusaki, I. Yasuda, J. Shimoyama, S. Yamauchi, K. Fueki, J. Electrochem. Soc. 140 (1993) 467–471.
[51] J. Deseure, Y. Bultel, L. Dessemond, E. Siebert, P. Ozil, J. Appl. Electrochem. 37 (2007) 129–136.
[52] T. Horita, K. Yamaji, N. Sakai, H. Yokokawa, A. Weber, E. Tiffee, J. Electrochem. Soc. 148 (2001) A456.
[53] A. Esquirol, N.P. Brandon, J.A. Kilner, M. Mogensen, J. Electrochem. Soc. 151 (11) (2004) A1847–A1855.